



**Nuno
Fortunato**

**Amostragem Por Caminho Aleatório Aplicado a
Modelos Vetoriais de Magnetismo
Random Path Sampling Applied to Vector Models
of Magnetism**

“That is not only not right, it is not even wrong.”

— Wolfgang Pauli



**Nuno
Fortunato**

**Amostragem Por Caminho Aleatório Aplicado a
Modelos Vetoriais de Magnetismo
Random Path Sampling Applied to Vector Models
of Magnetism**

Dissertação apresentada à Universidade de Aveiro para cumprimento dos requisitos necessários à obtenção do grau de Mestre em Física, realizada sob a orientação científica de Dr. João Amaral, Bolseiro de Pós-doutoramento de CICECO e Departamento de Física da Universidade de Aveiro e de Dr. João Gonçalves, Bolseiro Pós-doutoramento do Departamento de Física da Universidade de Aveiro

o júri / the jury

presidente / president

Ricardo Assis Guimarães Dias

Professor Auxiliar da Universidade de Aveiro

vogais / examiners committee

João Cunha de Sequeira Amaral

Bolseiro de Pós-doutoramento do Departamento de Física da Universidade de Aveiro (orientador)

Paulo Ivo Teixeira

Professor Adjunto com Agregação do Instituto Superior de Engenharia de Lisboa (arguente)

**agradecimentos /
acknowledgements**

My appreciation to Dr. João Amaral and Dr. João Gonçalves, for their supervision and transcendental patience in all matters. I thank Dr. Zsolt Gercsi, Dr. Karl Sandeman and Prof. Lesley Cohen at Imperial College London for the experimental data provided, as well as Prof. António Ferreira for his simulation data and Carlos Amorim for the nearest-neighbour tables used here. To my family for their support.

Abstract

O recém relatado Método de Monte Carlo de Amostragem por Caminho Aleatório (RPS) é aqui melhorado e a sua aplicação é estendida ao estudo dos modelos 2D e 3D Ising e Heisenberg discreto. A metodologia foi implementada para permitir o uso em infraestruturas de computação de alta-performance com base em CPU (C/MPI) e em computação paralela baseada em GPU (CUDA), com ganhos significativos de performance computacional. A convergência é discutida em termos da dependência da energia livre e magnetização em campo/temperatura.

A partir do cálculo da densidade conjunta de estados energia-magnetização, foram feitas computações rápidas das propriedades termodinâmicas dependentes do campo e temperatura. A transição emergente de 1^o ordem magneto-volumica no modelo de Ising compressível é interpretada usando a teoria de Landau de transições de fases.

Usando Gadolínio metálico como um exemplo real, é discutida a possibilidade de usar RPS como uma ferramenta para design computacional de materiais magnéticos. Propriedades experimentais magnéticas e estruturais de Gadolínio monocristalino são comparadas com cálculos baseados em RPS, usando parâmetros microscópicos obtidos por Density Functional Theory.

The recently reported Monte Carlo Random Path Sampling method (RPS) is here improved and its application is expanded to the study of the 2D and 3D Ising and discrete Heisenberg models. The methodology was implemented to allow use in both CPU-based high-performance computing infrastructures (C/MPI) and GPU-based (CUDA) parallel computation, with significant computational performance gains. Convergence is discussed, both in terms of free energy and magnetization dependence on field/temperature. From the calculated magnetization-energy joint density of states, fast calculations of field and temperature dependent thermodynamic properties are performed, including the effects of anisotropy on coercivity, and the magnetocaloric effect. The emergence of first-order magneto-volume transitions in the compressible Ising model is interpreted using the Landau theory of phase transitions.

Using metallic Gadolinium as a real-world example, the possibility of using RPS as a tool for computational magnetic materials design is discussed. Experimental magnetic and structural properties of a Gadolinium single crystal are compared to RPS-based calculations using microscopic parameters obtained from Density Functional Theory.

Contents

Contents	i
List of Figures	iii
List of Tables	vii
1 Introduction	1
2 Spin Models	3
2.1 Ising Model	3
2.1.1 Thermodynamics	4
2.1.2 Physical relevance	5
2.2 Heisenberg Model	5
2.2.1 Physical relevance	6
2.3 Other spin models	6
2.4 Analytical Methods	7
3 Monte Carlo Methods for Spin Models	8
3.1 Metropolis Method	8
3.1.1 Markov Chain	8
3.1.2 The Metropolis Algorithm	9
3.1.3 Critical Slowing Down	10
3.2 Histogram Methods	10
3.2.1 Single Histogram Method	10
3.2.2 Wang-Landau Method	11
3.3 Finite Size Effects	13
4 Introduction to the Random Path Sampling	14
4.1 Background	14
4.1.1 Algorithm	14
4.2 Implementation	17
4.2.1 CPU	17
4.2.2 GPU	17
4.2.3 Wall time comparison	18

5	Convergence and validation of RPS	20
5.1	Validation	20
5.2	Convergence	22
5.3	Fitting Free Energy	24
6	Application	27
6.1	Thermodynamics	27
6.2	Magnetocaloric effect	28
6.3	Compressible Ising Model	30
6.4	Magnetic Anisotropy Energy	33
7	Generalization of RPS to the Heisenberg Model	35
7.1	Introduction	35
7.2	Algorithm	37
7.3	Results	38
7.4	Comparison	40
8	Application of the Heisenberg model	42
8.1	Simulation of Gd	42
9	Conclusions	45
	Bibliography	46

List of Figures

3.1	Probability as function of energy of Ising SC Model L=16. The right-most peak ($K=0.221654$) is the measured distribution and the other two peaks are from varying the K value. Taken from [10].	11
3.2	Logarithm of the joint density of states $\ln(g(E,M))$ (on the left) and $M(T,H)$ curves (on the right) for the SC L=10 Heisenberg model. Taken from [29]. . .	12
3.3	Averaged absolute magnetization as function of temperature, for various sizes of the SC Ising Model. The grey arrow notes the theoretical T_c [20]. Simulation carried out using the ALPS package [21].	13
4.1	Scheme of the RPS algorithm.	14
4.2	The top graphs show the (E,M) histogram obtained for the Simple Square Ising L=6, with values normalized for each magnetization, on the left is the 3D representation and on the right the respective contour. The bottom plots are the Joint Density of States given by the graphs on top.	15
4.3	Plots for the mean value of the absolute magnetization $\langle M \rangle$ and M_{mF} magnetization from the $F(M,T)$ minima as a function of temperature.	16
4.4	Wall time for the SC lattice at L=4,6,8,10 as function of the number of spins. The black circles are the times and the dashed red line is the fit, with the corresponding parameters shown.	19
5.1	On the left, $\langle M \rangle(T)$ plots for the SC Ising model with N=232, with the Metropolis and RPS results overlaid. On the right, $M_{mF}(T)$ plot for the Ising L=6 SC in RPS and the $\langle M \rangle(T)$ curve for the L=100 lattice in Metropolis made using ALPS [21].	20
5.2	The predicted $M_{mF}(T)$ plots for the Ising model of different lattices, are shown on the left, with the theoretical T_c [20] indicated by arrows. The right plot compares the values for the DoS of the SS L=10 Ising model from RPS and analytical solution from the Beale method [37]. Inset is the deviation normalized by the analytical result.	21
5.3	On the top the logarithm of the DoS for M=0(left) and M=0.5(right), for the transfer matrix and RPS methods on SS L=8. The bottom plots are the respective normalized deviations of RPS from the transfer method.	21
5.4	Plot of the normalized deviation of the RPS estimated DoS from the analytical solution [37] for the Simple Square Ising L=8.	22

5.5	Shows the $F(M, T)$ isothermal curves for different degrees of convergence of the SC L=4 lattice, with the minima in respect to M denoted by a symbol. On the left 10^5 sweeps and on the right 10^9	23
5.6	On the left is $M_{mF}(T)$ curves corresponding to the converged 10^9 curve in red circles and as blue squares the 10^5 sweeps that is not converged. The right plot contrasts the 10^9 and 10^5 $F(M, T)$ to show the evolution of convergence. . .	23
5.7	The left-most plot shows the convergence of $\langle M \rangle(T)$ as a function of lattice sweeps. The centre is the $M_{mF}(T)$ curve at 10^{12} and 10^{13} sweeps, the corresponding plot for $\langle M \rangle$ is shown on the right side graph.	24
5.8	Left shows $F(M, T)$ curve at $T=5$ for different filter values for 10^6 and with a converged 10^9 run, with the minima in respect to M denoted by a symbol, the inset is the curve at the whole magnetization range. Right plot shows the corresponding $M_{mF}(T)$ curves.	24
5.9	$F(M)$ plots at the respective T_c , showing the noise of the curve, the inset shows the $M(T)$ curve with an arrow pointing to the T_c . On the right is the HCP lattice and the left is the BCC, both with 10^{11} repetitions and 128 spins. . . .	25
5.10	The $F(M, T)$ curves and their Landau fit for 10^6 (left) and 10^9 (right), the minima are shown by a square symbol for fit and circle for original curve. The insets are the zoomed in curve for $T=5$, that is denoted by the dashed box on the main graphs.	25
5.11	On the left the comparison of the fit at 10^6 runs and the corresponding $F(M, T)$ curve at 10^9 for $T=5$ (top) and $T=4.25$ (bottom). On the right, the respective magnetization curves.	26
5.12	Landau coefficients as a function of temperature for the SC L=4 Ising System, with expansion up to the 6th order.	26
5.13	Quality fit factor R^2 as a function of temperature. The deviation at low temperatures due to saturation is on the left. On the right, the peak corresponding to T_c is shown.	26
6.1	Plot of $M_{mF}(H, T)$ 3D curve of the L=6 Ising SC.	27
6.2	On the left, the $M(H)$ where the curves at the paramagnetic phase start at $M=0$, and ferromagnetic isotherms below $T_c=4.9$ have spontaneous magnetization. The centre plot are the isofield $M_{mF}(T)$ curves for SC L=6. The right plot is the respective Arrott plot showing H/M versus M^2 , the paramagnetic phase has curves that have $M^2=0$ when H/M is 0, implying that $M=0$ for $H=0$	28
6.3	The two plots contrast the ΔS_M from $\langle M \rangle$ (left) and M_{mF} (right), using Eq.6.3	29
6.4	On the left, the surface plot of the heat capacity per site with dependence on field and temperature. On the right, the corresponding ΔT_{ad} from $\langle M \rangle$ (right).	29
6.5	At the left, $M_{mF}(T)$ curves of the Ising SC L=6 for several elastic coefficients K for the same $J(\Delta v)$. On the right, the Bean-Rodbell model with $M(T)$ at different parameters η that depends on pressure, compressibility and T_c slope [44]. Above $\eta = 1$ the system has a 1st order transition.	31
6.6	The B coefficients of the Landau Expansion as function of temperature for various curves in Fig.6.5 for the Ising SC L=6.	31
6.7	Left graph shows the $M_{mF}(H)$ isothermal curves for Ising SC L=6, the red lines are the elastic system and the bashed blue lines are for the rigid system. The right side are the corresponding $M_{mF}(T)$ isofield lines.	32

6.8	The left plot shows the free energy as function of temperature, for the volumes before and after T_c of Fig.6.7. The right plot shows the volume transition for various K values, in Fig.6.5.	32
6.9	The volume and J behaviour in isothermal (left) and isofield (right) curves.	33
6.10	On the left, the $\Delta S_M(T)$ plot for the MCE effect from M_{mF} on the elastic SC L=6 lattice. On the right side the same for the rigid system.	33
6.11	On the far left, hysteresis loops for the SC Ising L=6 lattice for various temperatures. The other hysteresis loops show varying D values. On the middle is the system above T_c on the paramagnetic phase. The right plot corresponds to the ferromagnetic phase.	34
7.1	On the left the 6 direction discretization. On the right the 14 vector Heisenberg-like model.	35
7.2	On the left $F(M, T)$ curves for the SC L=3 Heisenberg Model, the squares mark the minima immediately before and after T_c , showing the discontinuous jump in magnetization. On the right is the corresponding $M_{mF}(T)$ curve.	36
7.3	On left most plot is the $\langle M \rangle(T)$ that shows the steep transition and the its respective $M_{mF}(T)$ plot on the centre left. The $\langle M \rangle(T)$ and $M_{mF}(T)$ plots on the centre right and far-right are for the filtered calculation.	39
7.4	Logarithm of the JDoS for the SC Heisenberg 14 model. The left side is the 3D plot and its corresponding contour is on the right.	39
7.5	$M_{mF}(T)$ plots for the HCP and SC Heisenberg 14-discretization, with filtering and Landau Fitting. The arrows indicate the theoretical T_c [51].	40
7.6	Both plots show the continuous Heisenberg model made in ALPS [21] and the Heis14 model with M_z in RPS (from M_{mF}) and $\langle M \rangle$ for Metropolis simulation. The right plot has the scale adjusted to better compare the curves.	41
7.7	$\langle M \rangle(T)$ plots for SC L=50 Heis14 with original and modified directions, from Metropolis simulations.	41
8.1	2x2x1 Gd supercell used for calculations. Made using VESTA [57].	42
8.2	On the left, the total energy dependency on volume for Gd. Right side are the J values for the in-plane and out-of-plane interactions as a function of c-axis variation.	43
8.3	The left graph is the field dependent behaviour of magnetostriction both from experimental measurements and simulation for Gd, at $T \approx 293$. On the right, the magnetic entropy variation as a function of field for the same temperatures.	43
8.4	The graphs show the experimental and simulated magnetization at different field-temperature values. On the left is the $M(T)$ plot and on right is the $M(H)$ plot.	44
8.5	On the left, the isofield curves of the magnetostriction as function of temperature for experimental and simulated data. The righth plot is the same for the variation in magnetic entropy.	44

List of Tables

4.1	Wall times for lattices on the Matlab, C and CUDA codes.	18
5.1	Values of T_c from RPS in the SS,SC,BCC, Face centred Cubic (FCC) and Hexagonal Closed-Packed (HCP) lattices. The corresponding analytical values are from the high temperature expansion method [20].	21
7.1	Orientations for the Heisenberg 14 model, the plane denotes the directions with equal M_z	36

Chapter 1

Introduction

This work explores the recently proposed method of Random Path Sampling (RPS), that allows solving a variety of vector models, with the advantage of evaluating the system in a field and temperature independent mode, allowing thermodynamic properties to be evaluated in a fast manner. The starting point for the discussion is the much studied Ising Model, that represents the prototypical example of phase transitions. A generalization to the Heisenberg model is then introduced and applied to explore the Magnetocaloric Effect (MCE) of Gadolinium.

Currently, ab initio methods are routinely used to determine properties of physical systems in a powerful fashion, with parameters such as exchange interaction and magneto-crystalline anisotropy being accessible. Thermodynamic properties are then obtained by combining these outputs with vector models. However, the methods available either require the computational effort to be expended to treat each point of the degrees of freedom (field and temperature), as in the Metropolis Algorithm; or are not readily accessible and rather complex, in the case of Wang-Landau. The RPS method was shown to allow an estimate the magnetization-energy dependent Density of States, and thus the partition function, the energy and other thermodynamic properties can be evaluated at any given temperature and field value.

The possibility of a fast, simple and general approach to describe the thermodynamics of magnetic systems, is not restricted to theoretical interest. Notably, the MCE has attracted interest as a potential eco-friendly and energy efficient cooling application. It will be later shown that a description of the MCE requires the system to be simulated for a variety of field and temperature values, that is readily accessible in RPS. High-throughput computational material design proposes combining thermodynamic simulations and first principles, along with databases and data mining to search for new materials. A general method to treat the thermodynamics could add an additional tool for estimation of properties of interest. Particularly, the optimization of material properties as function of the stoichiometry of substitutional alloys, replacing experimental workload with a fast and detailed computational study.

The structure of this work is as follows:

Chapter 2: An introduction to the general nature of the Spin Models later used, along with their physical significance, relevant thermodynamic quantities and related analytical methods.

Chapter 3: A short review of typical computational tools for the study of Spin Models is made, focusing on the Metropolis method and histogram methods.

Chapter 4: Introduces the general algorithm of Random Path Sampling along with the

computational details of the CPU and GPU implementations and their performance.

Chapter 5: The results of RPS are verified by comparing with Metropolis and methods that estimate Density of States. The particulars of convergence and quantities in Random Path Sampling are discussed. Improvements to convergence by filtering the sampling and fitting the free energy with Landau Theory are explored.

Chapter 6: The capabilities of the Random Path Sampling in calculating thermodynamic properties are exemplified in the Ising model. With the MCE and single-ion anisotropy being used as applications. The compressible Ising model as suggested by Domb is compared by the mean-field model of Bean-Rodbell.

Chapter 7: The generalization of RPS to the Heisenberg is introduced, along with the implementation. The effects of discretization are discussed based on the literature and Metropolis simulations by the author.

Chapter 8: A discretized compressible Heisenberg model is used to study the thermodynamics of Gadolinium as an application of Random Path Sampling. A comparison with experimental field and temperature dependent magnetization curves is made, along with the MCE and magnetostriction.

Chapter 2

Spin Models

The history and significance of the Ising and Heisenberg models are introduced, along with the relevant thermodynamic relations. The analytical methods available to study these models are also introduced.

2.1 Ising Model

Phase transitions are cooperative phenomena where the arrangement of the system (phase) changes due to modification of thermodynamic parameters like pressure or temperature, at a certain critical value. It is convenient to define an order parameter, that is an intensive quantity that changes at the transition from the most symmetrical phase to the least symmetrical or ordered phase. In a ferromagnet the order parameter is the magnetization.

The Ising model was introduced by Lenz in 1920, but its properties were only discussed in 1925 by Ising [2], in the 1D case. Ising showed that for a 1D chain of ferromagnetically coupled magnetic moments, that could each take up/down orientations a transition exists only at $T=0$ [3]. In addition, Ising considered next-nearest neighbour interactions, additional spin orientations and stacked linear chains.

The failure to reproduce ferromagnetic behaviour led to the not uncontroversial assumption by Ising that this would hold for the 3D case. Further, by the 1930's it had become clear that the model was at odds with the developing field of quantum mechanics and the newly proposed Heisenberg Model, leading to the general belief that the model lacked sufficient realism to describe magnetism [3].

In 1936 Peierls [4] showed that spontaneous magnetization was indeed possible for the 2D and 3D cases. There were also contemporaneous advances in the understanding of phase transitions. Namely, in alloys by Bragg and Williams [5] with later contributions by Bethe [6], in addition to Fowler's work on metal adsorption onto glass surfaces [7]. The eventual realization was these systems belong to the same class of phenomena and indeed it later turned out that the models were mathematically equivalent to the Ising model. The focus then changed to the study of the critical points, as to better understand cooperative behaviour [3]. This culminated with the analytical formula for the partition function of the Ising Model in the Simple Square lattice by Onsager [8], who also presented (without proof) the formula for spontaneous magnetization in 1949 [9].

The Ising model has since become one of the most published about physical models. It represents a simple case of a non-trivial phase transition and yet an analytical treatment of

the 2D case is known, making for a rare understanding of the exact behaviour of a model, opposite to the usually unknown detailed interactions in physical systems [3].

The Ising Hamiltonian describes a system of spins that take up/down (1/-1) directions, with an associated energy cost for parallel or anti-parallel nearest neighbour configurations such that

$$\mathcal{H} = -J \sum_{\langle ij \rangle} S_i \cdot S_j, \quad (2.1)$$

where J is the exchange constant and the sum is over the nearest neighbour pairs of the site labels i, j of the spins denoted S . If $J > 0$ parallel spins are energetically favoured and hence in ferromagnetic coupling, for $J < 0$ the system is anti-ferromagnetic and as such anti-parallel configurations are preferred. Additional energy terms can be added such as $-HM$, where H is an external magnetic field and $M = \sum_i^N S_i/N$ is the magnetization, or single-ion anisotropy $-D \sum_i^N S_i^2$.

2.1.1 Thermodynamics

The Ehrenfest classification groups phase transitions in orders based on the continuity of the thermodynamic potential. First order denotes that the first derivatives of thermodynamic potentials are discontinuous, for example entropy and magnetization. In turn, second order transitions have continuous potentials and first derivatives, with second order derivatives vanishing or going asymptotically to infinity, as is the case for specific heat [1].

The behaviour of an order parameter and thermodynamic functions near the critical point of a second order transition is in general described by critical exponents, in particular for a given function f the critical exponent λ is defined by

$$\lambda \equiv \lim_{\epsilon \rightarrow 0} \frac{\ln(f(\epsilon))}{\ln(\epsilon)} \quad \text{with} \quad \epsilon = \frac{T - T_c}{T_c}, \quad (2.2)$$

with f being continuous a positive for small values positive of ϵ . The values of these exponents have a high degree of universality, that is to say that they can be shared among different systems, forming an universality class.

Future discussion will focus on thermodynamic properties both defined from sampling of a simulation at equilibrium as well as based on partition function (Z) estimates, that can be obtained from the following relations. Defining $\beta \equiv 1/k_B T$ the probability of a state with energy E_i is

$$P(E_i) = \frac{g_i(E, M) e^{-E_i \beta}}{Z}, \quad (2.3)$$

$$Z = \sum_j g_j(E, M) e^{-E_j \beta}, \quad (2.4)$$

wherein the $g_i(E, M)$ is the Density of States (DoS) (the amount of possible states) as a function of E and M , denoted Joint Density of States (JDoS). By the definition of expectation value, it is possible to obtain the average $\langle E \rangle$ energy and internal energy U as

$$\langle E \rangle = \sum_i E_i P(E_i) = \frac{\partial \ln(Z)}{\partial T}, \quad (2.5)$$

$$U(T, H) = \sum_i E_i P(E_i | T, H). \quad (2.6)$$

$\langle E \rangle$ can be related to the heat capacity C_v by

$$C_v = \frac{d\langle E \rangle}{dT}, \quad (2.7)$$

$$\frac{\partial^2 \ln(Z)}{\partial \beta^2} = \langle E^2 \rangle - \langle E \rangle^2 = Var, \quad (2.8)$$

$$C_v = \frac{\langle E^2 \rangle - \langle E \rangle^2}{(k_B T)^2}. \quad (2.9)$$

It is then possible to obtain entropy from C_v using

$$S = \int \frac{C_v}{T} dT. \quad (2.10)$$

The Helmholtz free energy F in turn can be obtained from

$$F = -k_B T \ln(Z). \quad (2.11)$$

2.1.2 Physical relevance

Despite its simplicity the Ising Model is not merely a useful fiction to explore the physics of phase transitions, as it describes several physical systems [11]. Namely, a variety of short-range interactions belong to the 3D Ising universality class, that is to say they share the same critical exponents as the Ising Model.

Liquid-vapour transitions are described by the density ρ as the order parameter, at the point where the transition vanishes in the T - ρ phase diagram (the critical point), the transition is Ising-like. The system can indeed be mapped onto a Ising magnet Hamiltonian, but with corrections to scaling due to the different symmetry of the systems.

Similarly to the above case, an Ising-like behaviour is found in a variety of binary mixtures such as simple fluids, solids (as stated above for alloys) and even the more complex fluids of polymer blends and solutions of biological proteins. In this case the concentrations of the components serve as the order parameter. Other systems include ionic fluids that are thought to have a narrow window of Ising universality and micellar systems where surfactant molecules aggregate in aqueous solutions. The Ising universality class also plays a role in high energy physics, including several transitions in quantum chromodynamics [11].

The 2D Ising model also has experimental relevance, as it describes the criticality of some uniaxial antiferromagnets with anisotropy, along with disorder and structural transitions in surfaces and monolayers, for example hydrogen adsorbed in GaAs.

2.2 Heisenberg Model

In 1928 Heisenberg proposed a theory of ferromagnetism based on quantum mechanics, using the notion of exchange interaction he had previously obtained for Helium atoms. By combining Coulomb interaction with Pauli's exclusion principle, the resulting effect was strongly spin dependent and moreover had the correct dependency of the angle between spins, which the Coulomb interaction by itself could not reproduce [3]. In the following year, Dirac explicitly wrote the corresponding Hamiltonian

$$\mathcal{H} = \mathcal{H}_I + \sum_{i < k} \mathcal{H}_{ik} \frac{1}{2} [1 + (S_i, S_k)], \quad (2.12)$$

H_I and H_{ik} are the spin independent contributions and $(S_i, S_k) = S_{xi}S_{xk} + S_{yi}S_{yk} + S_{zi}S_{zk}$ are electron spins. Heisenberg himself succeeded in showing that Weiss's molecular-field theory of ferromagnetism [12] could be obtained, under the assumption that an equal exchange existed for all nearest-neighbour and that the exchange energies obeyed a Gaussian distribution. While not without criticism for these two assumptions, Heisenberg's theory was fast accepted as the explanation for ferromagnetism [3]. When only nearest neighbour interactions are considered the Heisenberg model is obtained as

$$\mathcal{H} = -J \sum_{\langle ij \rangle} \hat{S}_i \cdot \hat{S}_j \quad \text{with} \quad \hat{S} = \{S_x, S_y, S_z\} \quad \text{and} \quad |\hat{S}| = 1, \quad (2.13)$$

here \hat{S} is a classical spin that takes the form of a normalized vector that can take any orientation in 3D space. Since the Heisenberg Model has different magnetization components the conventional definition usually takes the form of $M = \sqrt{S_x^2 + S_y^2 + S_z^2}$. In contrast with the discrete Ising model, the Heisenberg model uses continuous degrees of freedom, thus energy differences can be infinitesimal allowing for excitations energetically close to the ground state [10]. While Heisenberg's theory is quantum mechanical, the above Hamiltonian is still classical, as it views spins as continuous variables as opposed to the Quantum Mechanical Heisenberg Model proper.

2.2.1 Physical relevance

Several ferromagnetic and antiferromagnetic materials fit into the critical universality class of the Heisenberg model, including Ni, Fe, Gd₂IC, Gd and La_{0.85}Ca_{0.2}MnO₃ [11].

The Heisenberg Model has been used as a predictive tool for properties like T_c , namely in systems where the moments are sufficiently large and localized [13]. The J value itself may be obtained by mapping energies from Density Functional theory, for example by using the Liechtenstein method [14]. In the interest of high-throughput computational material design for magnetic systems, the T_c is a fundamental property of interest [15].

2.3 Other spin models

In 1952 Potts proposed two vector models at the suggestion of Domb. The first was based on spins that take equably spaced in-plane vectors and interact in proportionality to their dot product. The second and now known as the q-states Pott model consists of spins that take states $S = 1, 2, \dots, q$ and have an associated energy of J between nearest neighbours that have the same state, as such has the Hamiltonian

$$\mathcal{H} = -J \sum_{\langle i,j \rangle} \delta_{S_i S_j}. \quad (2.14)$$

For $q > 2$ in 3D and $q > 4$ in 2D the transitions are of the 1st order, while $q=2$ returns the Ising Model, as only two directions are available. The Potts model has been used in Monte Carlo simulations of the magnetocaloric effects in Heusler alloys, for example in Ni₂Mn_{1-x}Cu_xGa [16].

When the Heisenberg model is restricted to x and y components one obtains the XY model,

$$\mathcal{H} = -J \sum_{\langle ij \rangle} \left(\hat{S}_{xi} \hat{S}_{xj} + \hat{S}_{yi} \hat{S}_{yj} \right). \quad (2.15)$$

While the above model does not have long range ordering, there are however topological excitations with a corresponding critical temperature [10]. Of physical interest for the model is the superfluid transition of ^4He in the λ -line that shares the XY 3D universality class, but also relates to superconductors and the Peierls transition in CuGeO_3 [11].

2.4 Analytical Methods

At present the exact partition function and thus all thermodynamic properties are known for the ferromagnetic Ising model in the Simple Square (SS) lattice, yet no such exact result exists for the Ising model in the Simple Cubic (SC) lattice. However, its possible to approximate the partition function of vector models using series expansions.

In a High-temperature expansion the partition function rewritten in the form of a Taylor series such that

$$Z = \sum_{n=0}^{\infty} \frac{(-\beta)^n}{n!} \sum_i E_i^n \quad (2.16)$$

wherein n is the index of the Taylor expansion and i denotes the sum over the energies. In particular for the vector models discussed above, the free energy per site f can be said to be

$$\beta f(K) = \sum_{n=0}^{\infty} a_n K^n, \quad (2.17)$$

where $K = J/k_B T$. At high-temperatures the series converges and can be used to obtain thermodynamic properties [17]. Expansions for a variety of lattices and models have been made, including Ising SC and Body Centred Cubic (BCC) as well the generic N-vector models [11]. Additionally, it has been used to estimate the T_c in the Heisenberg model for several lattices [18].

For models with discrete regularly spaced excitation energies the low-temperature series expansion can be made noting

$$Z = \sum_n e^{-\beta E_n} = e^{-\beta E_0} \left(1 + \sum_{n \neq 0} e^{-\beta \Delta E_n} \right), \quad \text{with } \Delta E_n = E_n - E_0. \quad (2.18)$$

The condition of the regularity implies that there must be an energy step such that $\Delta E_n = p\epsilon$ where p is an integer. The free energy per site can be determined to be

$$-\beta f(e^{-\beta\epsilon}) = -\beta \frac{E_0}{N} + \sum_{n=1}^{\infty} a_n e^{-n\beta\epsilon}, \quad (2.19)$$

as T goes to zero $e^{-\beta\epsilon}$ vanishes and as such the series converges at low temperature. This method was used to calculate the energy distribution for the finite SS Ising model by Beale [19].

Several other series approximations exist such as molecular-field theory [20], zero-temperature and thermodynamic perturbations [17]. Of note is that the molecular-field theory does not belong to the same universality class of the Ising model, as it is a mean-field theory and thus belongs to that class of universality.

Chapter 3

Monte Carlo Methods for Spin Models

A short review of some relevant numerical methods applicable to the Ising and Heisenberg Models is made below. The central concept of Markov chains is approached, along with the Metropolis Method and Wang-Landau Methods, among others.

3.1 Metropolis Method

3.1.1 Markov Chain

The basis for the methods discussed in this chapter is the concept of Markov chains and the closely related master equation.

Let X_{t_n} be the state randomly taken by the system at time n , chosen among a finite set of states $S_{\{1\dots i\}}$. A process is a Markov chain if the probability of X_i taking a particular state depends only on the state of X_{i-1} and not previous states of the system. In other words, the conditional probability of $X_i = S_{i_n}$ based on its full history,

$$P(X_{t_n} = S_i | X_{t_{n-1}} = S_{i_{n-1}} | \dots | X_{t_1} = S_{i_1}), \quad (3.1)$$

must be equal to the conditional probability in respect to just the previous step

$$P(X_{t_n} = S_i | X_{t_{n-1}} = S_{i_{n-1}}). \quad (3.2)$$

It is suitable to define the latter as the transition probability from state i to j denoted W_{ij} such that

$$W_{ij} = P(X_{t_n} = S_j | X_{t_{n-1}} = S_i). \quad (3.3)$$

The standard properties of probability apply here, to the effect that $\sum_j W_{ij} = 1$ and $W_{ij} \geq 0$. Taking the time dependence as continuous, the change in the probability of the system being at a certain state S_j is given by the master equation

$$\frac{dP(S_j, t)}{dt} = \sum_i W_{ij} P(S_i, t) - \sum_i W_{ji} P(S_j, t), \quad (3.4)$$

that can be interpreted as the balance between transitions that move into and out of state j . We will later see the significance of this equation within Monte Carlo importance sampling such as the Metropolis Algorithm.

3.1.2 The Metropolis Algorithm

If a simulation that follows a Markov chain is at equilibrium, then the $\frac{dP(S_j,t)}{dt}$ term in the master equation (Eq.(3.4)) must vanish and as a result one obtains the so called detailed balance condition

$$P_{eq}(S_j)W_{ji} = P_{eq}(S_i)W_{ij}. \quad (3.5)$$

This relates to Metropolis as any importance sampling must have a probability distribution that obeys the detailed balance condition, so that the process is a Markov chain. The thermodynamic probability distribution of state i with energy E_i is

$$P_i(t) = \frac{e^{-E_i/k_B T}}{Z}, \quad (3.6)$$

however the partition function is not always known. This motivates the requirement that the sampling follows a Markov process, given that in a Markov chain the probability of obtaining a state is built on the previous state the problem of an unknown Partition function is overcome. The transition probability is then the ratio of the probabilities of the two states or

$$W_{ij} = \frac{1}{\tau_0} e^{-\Delta E/k_B T}, \quad (3.7)$$

wherein $\Delta E = E_j - E_i$ and τ_0 is the attempt time of the spin flip, that can be set to 1. This distribution allows for a local energy increase ($\Delta E > 0$), with some probability, due to thermal excitation dependent on $k_B T$, while a decrease in energy ($\Delta E < 0$) is always preferred. Thus the probability of a spin flip is $\min(1, e^{-\Delta E/k_B T})$. The Metropolis algorithm [22] for the Ising model obeys the above transition probability so that the system reaches an equilibrium and desired quantities such as energy or magnetization can be sampled. This is done by employing the following steps:

1. The lattice is set at an initial state and (T, H) are defined;
2. A spin is chosen and the energy difference between the initial and flipped states ΔE is calculated;
3. The probability of accepting the flip is then $\min(1, e^{-\Delta E/k_B T})$;
4. The resulting value for the thermodynamic properties of interest is noted;
5. Steps 2 and 3 are repeated as desired.

The system requires a sufficient amount of steps to reach an equilibrium (thermalization), as such a number of states should be discarded before starting the averaging of thermodynamic variables. Typically, the unit of steps is the MC/step corresponding to an amount of trial flips equal to the number of spins (N) [10]. The average over R trials of a variable such as magnetization is given by $\langle M \rangle = \sum_i M_i / R$. However, the usual thermodynamic variable looked at is the $\langle |M| \rangle = \sum_i^N |M_i| / N$, in consequence of $-M$ and M being degenerate (for null H) and thus making the averaged value vanish when the system repeatedly switches between the two states. An analogous procedure can be carried out for the Heisenberg model:

1. The lattice is at an initial state with a (T, H) ;

2. A random orientation that will be the final state of the flip is generated;
3. The ΔE for the flip is found for the chosen site;
4. The probability of accepting the flip follows $\min(1, e^{-\Delta E/k_B T})$
5. The new thermodynamic variables are stored;
6. Steps 2 and 3 are repeated as desired.

3.1.3 Critical Slowing Down

At a given temperature clusters of parallel spins form up to a certain maximum size, this is called the correlation length ξ . Near T_c ξ diverges to infinity resulting in long temporal correlations [23], that is to say the states are correlated for a large amount of MC/steps. To elucidate this point it is useful to consider time-dependent correlation functions ϕ at equilibrium

$$\phi_{MM}(t) = \frac{\langle M(0)M(t) \rangle - \langle M \rangle^2}{\langle M^2 \rangle - \langle M \rangle^2}. \quad (3.8)$$

The asymptotic behaviour of $\phi(t)$ at large t is an exponential decay $\phi(t) \rightarrow e^{-t/\tau}$, where τ is the correlation time. Near T_c the critical behaviour of τ follows a power law

$$\tau \propto \xi^z \propto \epsilon^{-\nu z} \quad (3.9)$$

where ν is the dynamic critical exponent [10]. This relation is of practical importance in Metropolis simulations, as it dictates the speed of convergence near T_c for the averaged quantities. The essential picture is that a single flip update becomes unlikely when large clusters are present, as only the spins at the borders of the clusters are likely to be flipped [23].

To address critical slowing down cluster methods like the Swendsen-Wang [24] and Wolff[25] Algorithms have been developed. The basis of these is to map the ferromagnetic spin system into a percolation problem that does not suffer from critical slowing down. By defining bonds between spins within a cluster with a certain probability and flipping the bonded spins the resulting state is uncorrelated with the initial state. These methods are said to do global updates as opposed to the local Metropolis flip.

3.2 Histogram Methods

3.2.1 Single Histogram Method

The Single Histogram method adds additional information to Monte Carlo simulations by estimating the density of states from the obtained configurations [10]. It is possible to write the probability of a configuration with a given magnetization and energy at the chosen temperature T_0 as

$$P_{K_0}(E^*, M) = \frac{1}{Z(K_0)} g(E^*, M) e^{-K_0 E^*} \quad (3.10)$$

where K_0 is $J/k_B T_0$ and E^* is the dimensionless energy ($\sum_{\langle ij \rangle} \hat{S}_i \cdot \hat{S}_j$) and $Z(K_0)$ is the Partition Function at T_0 . Hence, by making a histogram of the frequency of (E^*, M) configurations in N trials denoted $h(E^*, M)$, $P_{K_0}(E^*, M)$ can be approximated by $h(E^*, M)/N$. It

is then possible to find the approximation of density of states as

$$g(E^*, M) = h(E^*, M) \frac{Z(K_0)}{N} e^{K_0 E^*}. \quad (3.11)$$

Since any coupling value K has a $P_K(E^*, M)$ analogous to Eq.3.10, the following relationship can be established,

$$P_K(E^*, M) = \frac{h(E^*, M) e^{(K-K_0)E^*}}{\sum_{E^*, M} h(E^*, M) e^{(K-K_0)E^*}}, \quad (3.12)$$

allowing for estimation of density of states away from the initial point of measurement K_0 . Ferrenberg and Landau [26] used the Single Histogram to do a precise study of the critical behaviour of the 3D Simple Cubic Ising Model, by taking advantage of the possibility of varying K . The variation of K is however limited for a finite sampling. Since $h(E^*, M)$ is limited to configurations that are likely to appear at K_0 , when the histogram of K is no longer well described by the configurations of K_0 , the shift in K is no longer valid. In particular, the peak of the K -value distribution will be shifted towards the sides of the K_0 histogram, i.e. where the sampling is smaller and thus statistically uncertain, as can be seen in Fig.3.1.

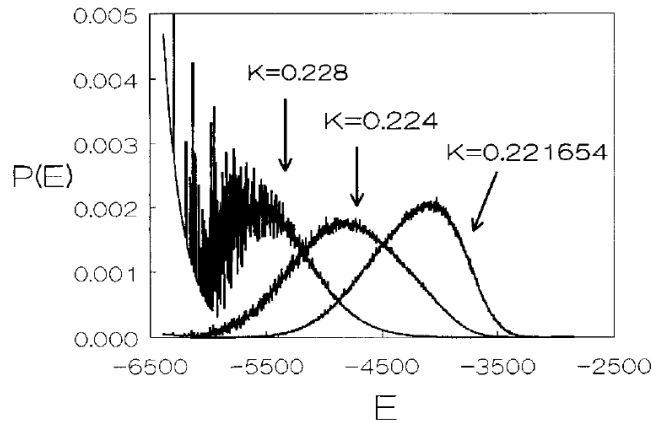


Figure 3.1: Probability as function of energy of Ising SC Model $L=16$. The right-most peak ($K=0.221654$) is the measured distribution and the other two peaks are from varying the K value. Taken from [10].

It is possible to generalize and to modify the Single Histogram Method. In the Multi-Histogram Method several histograms at differing K points are suitably combined with aim at increasing the range of valid K values.

3.2.2 Wang-Landau Method

In Wang-Landau sampling [27] an estimate of the partition function is made by noting that

$$Z = \sum_E g(E) e^{-E/k_B T}, \quad (3.13)$$

and iteratively calculating the density of states $g(E)$ (DoS) from the condition of a flat histogram, i.e all states are visited with equal probability [10]. For a random walk over the energy space of a system there is a statistical distribution N that dictates the acceptance of

a step(flip). If the histogram is to be flat, the rule for accepting a flip such that $E_j \rightarrow E_i$ will be in the form $\min(1, N(i)/N(j))$. The distribution $N(i)$ must be proportional to $1/g(E_i)$, so that the probability of visiting microstates with energy E_i is equal between them. It follows that the condition of a flat histogram implies that $g(E)$ is known.

The procedure for the Wang-Landau Method, starts by setting $g(E_i)$ to 1. A flip at site i from state with E_1 to one with E_2 is given by

$$P(E_1 \rightarrow E_2) = \min\left(\frac{g(E_1)}{g(E_2)}, 1\right), \quad (3.14)$$

if the flip is accepted then $g(E_i)$ is set to $g(E_i) * f_i$, where f_i is the so called modification factor and initially is greater than 1. This is then repeated until the histogram for the energy states reaches a desired flatness, the process is restarted with an $f_{i+1} < f_i$ with the previous $g(E)$ as the starting point. The iteration continues until f is sufficiently low e.g. 10^{-8} [10]. Using the partition function with the obtained DoS, it is possible to calculate the desired thermodynamic properties.

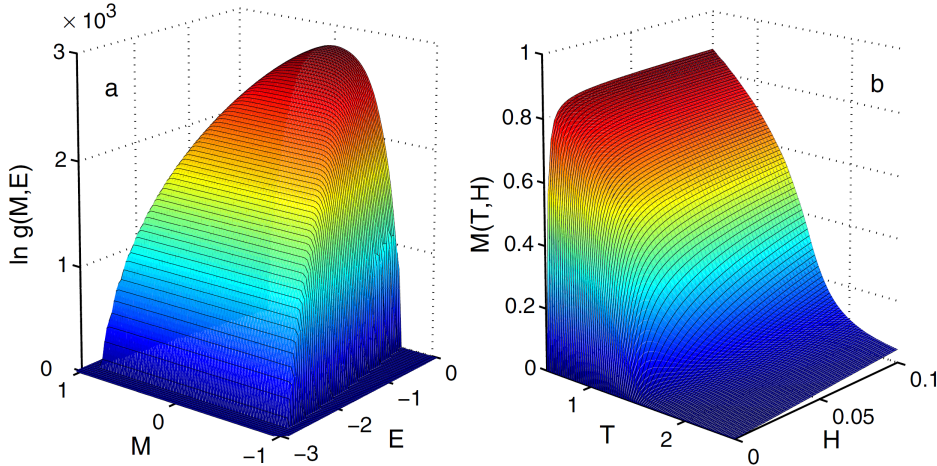


Figure 3.2: Logarithm of the joint density of states $\ln(g(E, M))$ (on the left) and $M(T, H)$ curves (on the right) for the SC $L=10$ Heisenberg model. Taken from [29].

While the description above follows the original application of Wang-Landau that used $g(E)$, several extensions have been presented. Of natural interest is the calculation of the joint density of states $g(E, M)$, the advantage being that magnetization dependent energy contributions such as magnetic field H can be accounted for without a simulation for each particular H value. Using the general nature of JDoS Tsai et al. [28] constructed a (H, T) phase diagram for the triangular asymmetric Ising model.

Zhou et al. [29] generalized the method to include continuous variable and simulated the $L=10$ Simple Cubic Heisenberg model. The magnetization used for the JDoS was the sum over the S_z component and not the usual quantity of $M = \sqrt{S_x + S_y + S_z}$. An additional consideration was the use of binning of possible energies and magnetizations, with interpolation between bins and a global update function instead of a single flip update. Fig.3.2 shows the obtained JDoS and magnetization curves by Zhou et al.

Additional applications of Wang-Landau are the simulation of fluids, polymers, liquid crystals, binary Lennard-Jones glass among others [28].

LSMS

An application of the Wang-Landau is the locally self-consistent multiple scattering (LSMS), that combines Density Functional Theory with Wang-Landau to describe thermodynamic behaviour based on the energy of a quantum mechanical treatment of the system. LSMS takes the approach of directly obtaining the thermodynamics, without the need of a vector model. As previously, a DoS estimate is made iteratively by constructing a flat histogram of the energy states and picking sites to attempt flips. However, the LSMS uses DFT to calculate the Green function and the corresponding energy of the state and returns that value. The magnetic moments can take any orientation and need not be collinear.

Brown et al. [30] carried out a calculation for iron (body-centred cubic lattice) for up to 250 atoms, using 4886720 hours of computation on a supercomputer. The obtained T_C of 980K was close to the experimental value 1050K, but the specific heat was not completely well described as the Wang-Landau algorithm favoured sampling high energy states and complete convergence would be computationally prohibitive.

3.3 Finite Size Effects

As all simulations are carried out for finite lattices the effects of size need to be considered. An immediately noticeable effect is a 'smearing' (broadening) of the transition in respect to temperature, resulting in higher T_C values. Fig.3.3 shows the evolution of the mean absolute magnetization $\langle |M| \rangle(T)$ for different lattice sizes of the SC Ising model, with the arrow indicating the theoretical T_C for the infinite lattice. It is possible to study the finite size scaling of a lattice, a useful application of this is to distinguish between first and second order transitions, regardless of the always smooth nature of a transition at finite sizes and to extrapolate the critical exponents of infinite lattices from finite size simulations[10].

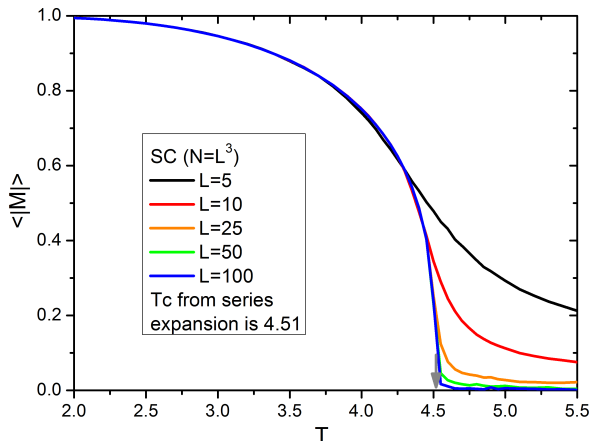


Figure 3.3: Averaged absolute magnetization as function of temperature, for various sizes of the SC Ising Model. The grey arrow notes the theoretical T_C [20]. Simulation carried out using the ALPS package [21].

Chapter 4

Introduction to the Random Path Sampling

In this chapter a general introduction to the Monte Carlo method of Random Path Sampling (RPS) is given, focusing on its algorithm and on the nature of the workflow. The implementations for CPU (C code) and GPU (CUDA/C) are briefly discussed and later compared to a previous Matlab code by Dr. João Amaral.

4.1 Background

In the original paper on RPS by Amaral et al. [31] the partition function was estimated for the Simple Square Ising model. The convergence of the $\langle |M| \rangle$ was studied for up to 64 spins, it was found that $\sqrt{2^N}$ sweeps over the lattice was sufficient for convergence of 0.1%. Additionally, $\langle |M| \rangle(H)$ and change of entropy with field for rigid and compressible lattices were presented.

4.1.1 Algorithm

In theory, it would be possible to get the exact partition function by visiting all configurations of the system and building a (M, E) histogram. Thus one would know the total amount of states at each magnetization and energy which is the JDoS and the partition function could then be calculated. However, the number of states scales as 2^N , making the generation of all configurations intractable even for a small amount of N spins.

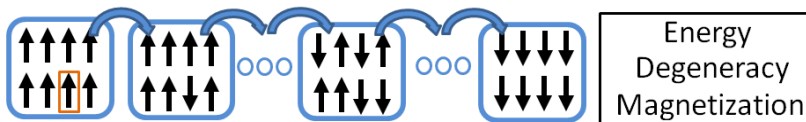


Figure 4.1: Scheme of the RPS algorithm.

RPS makes an estimate of the JDoS via a sampling of states that is flat in magnetization, obtained from spin flips that follow a random sequence of the lattice sites. The system is taken from the all spins up state (M) to the all down ($-M$) and a histogram with the number of states for each of the possible magnetization-energy pairs is kept. The procedure is pictured

in Fig.4.1. This is similar to visiting all possible states, however in RPS only the generated states are considered as part of JDoS. The key is then to obtain states that are not biased towards a particular set of E or M values, in a computationally affordable fashion. The use of a random sequence for flips allows the generation of unbiased states. It is however natural to ask why would one follow a path sampling and not simply generate random configurations, for example by rearranging a fixed number of spins that are up and down. As the start is a known state, the energy calculation is for the local energy difference from each flip, making it computationally more advantageous. Random configurations would require the calculation of the local energies for the N spins and give information for only one configuration. We will later discuss the particulars of the nature of this sampling and its convergence as well as possible improvements.

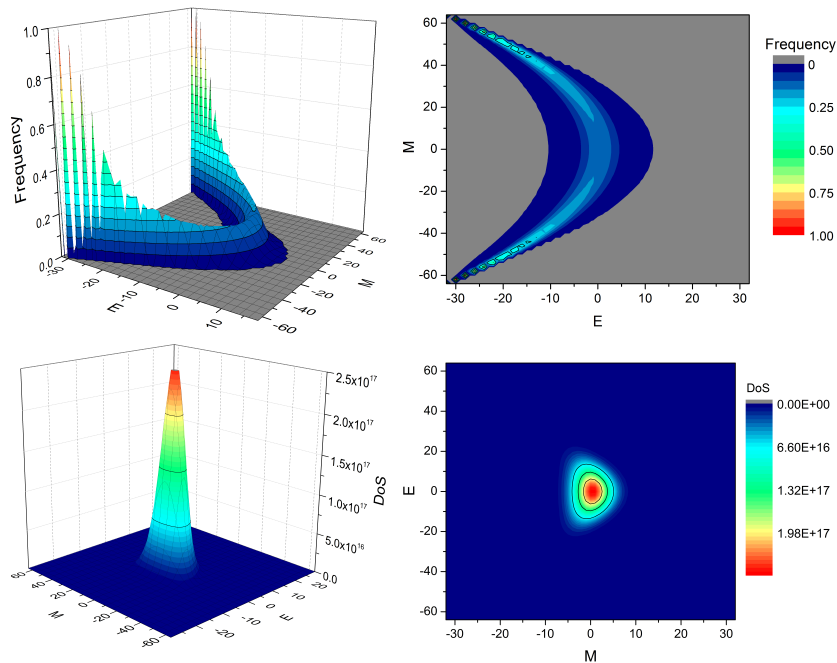


Figure 4.2: The top graphs show the (E,M) histogram obtained for the Simple Square Ising $L=6$, with values normalized for each magnetization, on the left is the 3D representation and on the right the respective contour. The bottom plots are the Joint Density of States given by the graphs on top.

It is possible to calculate the joint density of states (JDoS) denoted $g(E, M)$ from the histogram $h(E, M)$, by noting that for a large number of R trials

$$\frac{h(E, M)}{R} \rightarrow P(M, E), \quad (4.1)$$

$$P(M, E)\Omega(M) \rightarrow g(M, E) \quad (4.2)$$

$\Omega(M)$ being the number of possible configurations with M magnetization. The typical resulting histogram is shown on the top plots of Fig.4.2, while the bottom figures are the resulting JDoS plots. The overall shapes of these plots will depend not only on the underlying JDoS of the model, but also on how the method converges, this will be discussed later on. The

$h(E, M)$ plot will tend to be symmetric as convergence is achieved, as such it is sufficient to take the system from M to 0 magnetization and mirror the energy values along the $M=0$ axis.

For the Ising Model the calculation of $\Omega(M)$ is simply the determination of the possible combinations with the given number of up and down spins N_\uparrow and N_\downarrow respectively, $\Omega(M)$ can then be written as

$$\Omega(M) = \binom{N}{N_\downarrow} = \frac{N!}{N_\downarrow!(N - N_\downarrow)!}, \quad (4.3)$$

$$N_\downarrow = \frac{(N - M)}{2}. \quad (4.4)$$

The estimate of thermal properties is then made by considering the partition function in the form

$$Z = \sum_i \sum_j g(E_i, M_j) e^{\frac{E_i - HM_j}{T k_B}}, \quad (4.5)$$

it should be noted that the E term above depends only on the exchange interactions and is not the total energy. The advantage here in using $g(E, M)$ and not $g(E)$, is that the histogram becomes independent of the $-HM$ term and any other homogeneous energy terms, for instance single-ion anisotropy. It is thus computationally inexpensive to estimate the partition function at any desired field, by merely re-evaluating Eq.(4.5). Adding to this, by estimating the partition function from the JDos, the free energy for a pair (T, M) values can then be calculated by using the previously introduced Eq.(2.11)

$$F = -k_B T \ln(Z). \quad (4.6)$$

Using the free energy as $F(T, M)$, it is then possible to introduce a novel quantity here denoted as M_{mF} . That is obtained by finding the M values that minimize F at a certain T . The resulting magnetization is a different property from the averaged values, as calculated by Metropolis and DoS estimating methods. Fig. 4.3 compares M_{mF} and $\langle |M| \rangle$ curves for the Ising SC $L=4$ and shows that the M_{mF} transition is noticeably less smeared than the $\langle |M| \rangle$ curve.

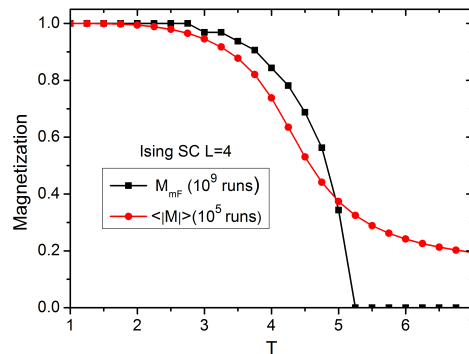


Figure 4.3: Plots for the mean value of the absolute magnetization $\langle |M| \rangle$ and M_{mF} magnetization from the $F(M, T)$ minima as a function of temperature.

4.2 Implementation

4.2.1 CPU

A notable feature of RPS is that it is embarrassingly parallel, as paths can be separately executed and their histograms joined later on, opening the doors for parallel and even distributed computation.

The general work-flow is to first generate individual histograms for a sizeable number of sweeps (typically a 10^9 run) on each core using C code. The separate runs are then combined by means of the *unique* function in Matlab and the final histogram is saved. A Matlab script is then used for evaluating the partition function and thermodynamic properties.

The main function in the C program is shown below in pseudocode.

```

let  $h$  be a vector that has all  $(M, E)$  combinations;
for  $k$  < number of runs do
  create random permutation of lattice sites;
  for  $i$  < size lattice do
    let  $r$  be the  $i$ -th spin in the permutation;
     $s[r] \leftarrow -1$ ;
    calculate new  $E$  from flip;
     $M \leftarrow M+1$ ;
     $h(M, E) \leftarrow h(M, E)+1$ ;
  end for
end for
Print non-zero histogram entries and their E,M values.

```

The random permutations are made using Fisher-Yates shuffling that follows the algorithm:

```

Initialize  $sq$  vector with spin labels;
 $j \leftarrow$  size lattice-1;
for  $j$  from 0 to size lattice-2 do
  generate a random number  $k$  within  $[0, j]$ ;
   $sq[j] \leftrightarrow sq[k]$ .
end for

```

The pseudo-random number generation is made using the Mersenne Twister Algorithm, as implemented in the "SIMD-oriented Fast Mersenne Twister" program (SFMT) [32].

The original C version of the code was made to be executed individually in each core. However for calculations made using the cluster at the Physics Department of the University of Aveiro an MPI parallelized code was used. Given the completely parallel nature of RPS, the MPI code was only sequential during the initial assignment of variables, with each core then running the RPS algorithm independently.

4.2.2 GPU

While the algorithms for the CPU and GPU codes are fundamentally the same, the implementations differ due to the nature of the different architectures. Before addressing the specifics of the GPU code, a small introduction to CUDA and Graphics Processors will be

given. The interest in GPU code lies in the potential to exploit the parallel nature of the hardware architecture and raw throughput. At first glance these characteristics agree well with RPS, as it is embarrassingly parallel and requires a large number of sweeps. For the Metropolis Algorithm with sequential updates, speed-ups of up to two orders of magnitude are reported [33][34] and one order for Wang-Landau[34], which further motivated the interest in GPU code.

Computation in GPUs are carried out by several Streaming Multiprocessors (SM), each containing a number of Streaming Processors (SP) that have their own registry memory and can access a shared memory. The SM can communicate with its cache and the on-chip global memory (analogous to RAM), along with other types of memory [35]. The architecture of a GPU is then itself parallel at a computational and local memory level, this will impact how the program itself works. The basic entity in CUDA are threads that are grouped into a warp, that runs concurrently, these then are further bundled into blocks. It is important to keep in mind that while threads can work and access their local memory in parallel, reads and writes for the same address in shared memory must be sequential to avoid errors.

The GPU code first calls a random number generating function, where threads with optimized block size and number fill a vector with random lattice indexes. The random numbers are made by a Mersenne Twister generator as implemented in the CUDA toolkit [36]. A Fisher-Yates function then allocates a continuous array sized $N * (\text{number of threads})$ in global memory and each thread then applies the Fisher-Yates algorithm in its respective 'slice' of the array. The flips and energy calculations are again done as in the CPU code but in several lattices concurrently. However, saving to the histogram vector is not done in parallel, as to avoid contention of a thread reading a value that is then updated by another one and then making an update based off the previous value.

4.2.3 Wall time comparison

Table 4.1 gives the wall time (real time of the task) for 10^9 sweeps on each of the different codes for various lattices. The GPU used was a GeForce GTX 760 and the CPU was a Intel i7-4770K @ 3.5GHz with 4 physical cores. The C code times are presented assuming the use of all the cores in independent calculations and the time is then divided by the number of cores, which is representative of real world use, as opposed to single core performance.

Table 4.1: Wall times for lattices on the Matlab, C and CUDA codes.

Lattice	Number Spins	Matlab	CUDA (GPU)	C
Simple Square	100	—	8m	3m40s
Simple Cubic	216	302m	—	5m
Body Centred Cubic	128	224m	18m	3m40s
Body Centred Cubic	432	803m	66m	11m
Closed Pack Hexagonal	128	270m	22m	11m

Mention must be made that the Matlab code has a significantly different workflow. The E values are saved into an array that is sectioned by magnetization and a unique function coalesces the entries into $h(E,M)$ histogram with the observed values. Great care was taken by Dr. Amaral in vectorizing the operations and the above wall times are from optimized code. In practice, the unique function in the Matlab library will sort the pairs and count

over equal pairs, outputting their frequency. The sorting of a large array is the bulk of the computational expense, and the use of a histogram in CUDA and C codes was chosen to avoid this. The same methodology in the form of C code will be tested further on, in the context of the Heisenberg vector model.

Overall, both C and CUDA codes are limited by memory speed, limiting further optimizations. In the case of CPU code the write to the histogram accounts up to 80% of the run time. In the GPU, the memory limitation is compounded by the inefficiency of the serial operation for updating the histogram. In general, workloads that are compute bound, rather than limited by memory stand to be the most benefited by GPU parallelization. Future CUDA code must work around the use of a global histogram to avoid the serial write speed bottleneck. This could be done by allocating several histograms that are kept in local memory and later on combined.

Alternatively, the use of a sort and count methodology might be an alternative to best utilize the higher throughput of GPU's, as it is more computationally taxing and less memory reliant. Although the total number of writes for a unique type code is always larger than the histogram method, the initial construction of the E array is quite faster than saving to a histogram. When writing to a histogram the energy positions will be random and a new section of the histogram must be recalled from RAM into cache. Additionally, this randomness makes prefetching to cache impossible, that is to say the compiler (or the coder using compiler intrinsics) cannot request that the relevant section of RAM be brought into cache ahead of time to hide the read times. Even attempting to prefetch by making a reasonable guess to the location of the next energy position did not provide a noticeable improvement for the C code.

The scaling of the wall time with the system size for the SC lattice $L=4,6,8,10$ is shown in Fig.4.4 along with a linear fit, demonstrating that the time dependence is linear with lattice size.

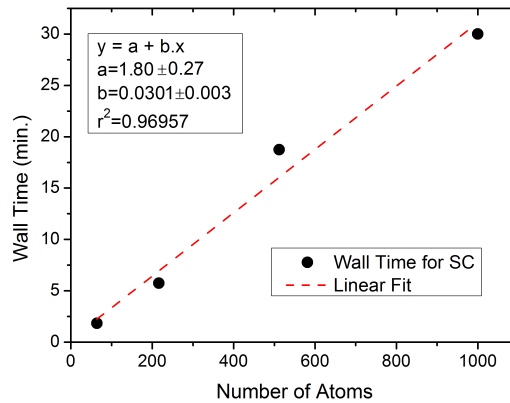


Figure 4.4: Wall time for the SC lattice at $L=4,6,8,10$ as function of the number of spins. The black circles are the times and the dashed red line is the fit, with the corresponding parameters shown.

Chapter 5

Convergence and validation of RPS

The following sections discuss the details behind RPS. Firstly, how convergence can be tested and ways to improve it are addressed. Results for the Simple Square and Simple Cubic lattices are compared with Metropolis simulations and analytical methods.

5.1 Validation

As was shown in the original paper by Amaral et al. [31], RPS can reproduce the $\langle |M| \rangle(T)$ behaviour of the SS Ising model. This is easily extended to the 3D lattices, such as SC.

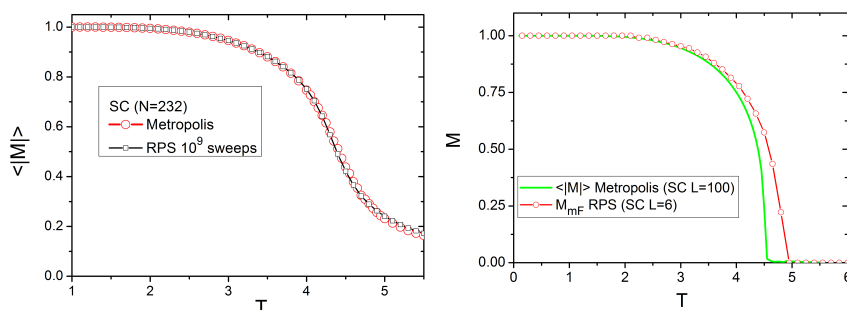


Figure 5.1: On the left, $\langle |M| \rangle(T)$ plots for the SC Ising model with $N=232$, with the Metropolis and RPS results overlaid. On the right, $M_{mF}(T)$ plot for the Ising $L=6$ SC in RPS and the $\langle |M| \rangle(T)$ curve for the $L=100$ lattice in Metropolis made using ALPS [21].

The left side of Fig.5.1 shows how the Metropolis simulated SC $L=6$ lattice matches well with the RPS results, while the right plot compares the $L=100$ SC $\langle |M| \rangle$ using Metropolis and the magnetization from the minimum of the free energy M_{mF} in RPS for $L=6$ SC. As previously mentioned the M_{mF} transition is less broad than the $\langle |M| \rangle$ equivalent at the same size, and the T_c differs due to finite size effects.

The values for the T_c 's of various lattices from RPS are enumerated in Table 5.1, with the respective infinite lattice T_c from series expansions [20]. All simulated values agree well, keeping in mind the finite size effects on the T_c . The corresponding $M(T)$ curves are in left plot of Fig.5.2, with the theoretical values of T_c as arrows.

Table 5.1: Values of T_c from RPS in the SS,SC,BCC, Face centred Cubic (FCC) and Hexagonal Closed-Packed (HCP) lattices. The corresponding analytical values are from the high temperature expansion method [20].

Lattice	Size	Number Sites	T_c	Infinite Lattice T_c	$\Delta T_c(\%)$
SS	10	100	2.85	2.27	25.56%
SC	6	216	4.95	4.51	9.76%
BCC	6	432	6.95	6.35	9.45%
FCC	5	500	10.8	9.79	10.32%
HCP	5	500	10.4	≈ 10	-

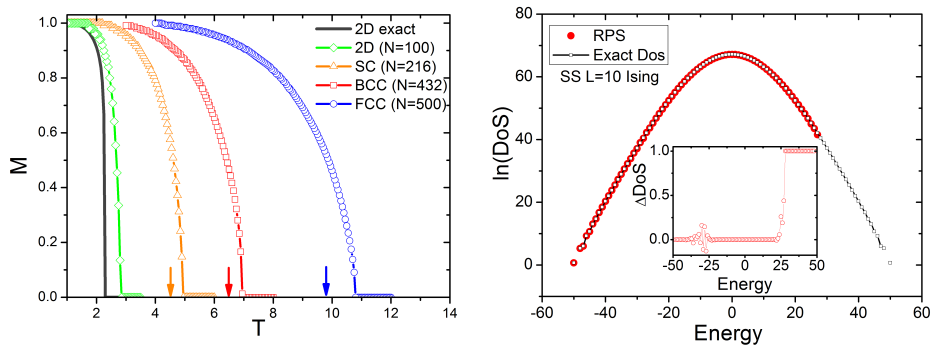


Figure 5.2: The predicted $M_{mF}(T)$ plots for the Ising model of different lattices, are shown on the left, with the theoretical T_c [20] indicated by arrows. The right plot compares the values for the DoS of the SS L=10 Ising model from RPS and analytical solution from the Beale method [37]. Inset is the deviation normalized by the analytical result.

The logarithm of the DoS from RPS in the SS lattice is presented on the right of Fig.5.2, with the analytical solution overlaid and with the difference between values shown in the inset. The DoS is well reproduced despite the density of states being as high as 10^{29} and only 10^{12} lattice sweeps were made. The analytical solution was obtained from a low-temperature series expansion of the partition function of a finite lattice [19] using the Mathematica code [37].

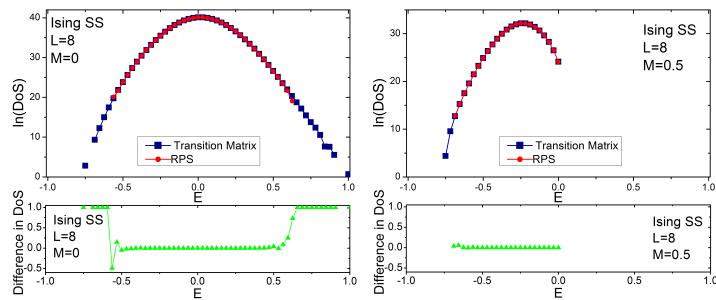


Figure 5.3: On the top the logarithm of the DoS for $M=0$ (left) and $M=0.5$ (right), for the transfer matrix and RPS methods on SS $L=8$. The bottom plots are the respective normalized deviations of RPS from the transfer method.

To further test RPS the DoS at specific magnetizations is compared with the results from

the transition matrix Monte Carlo method, that were provided by Prof. António Ferreira and used in reference [38]. In short, the simulation sampled a flat energy-magnetization histogram, using the transition matrix method [[39],[40]], that estimates the probability of a given state $\sigma(E, M)$ transitioning to the possible states $\sigma'(E', M')$ using Monte Carlo methods, in this case utilizing the acceptance probability in infinite-temperature. The agreement of the DoS from RPS and the transition matrix calculation for the L=8 SS lattice is show in Fig.5.3, along with the deviation of RPS from the transfer matrix method, normalized by the transfer matrix value at each energy point.

5.2 Convergence

Given that RPS generates states randomly, there is no guarantee of visiting lower probability states aside from a large sampling. To the effect that the sampling of these low probability states is the slowest to converge. It is possible to see how convergence evolves comparing the analytical solution of the DoS with the values obtained by RPS. Fig.5.4 shows the deviation of the DoS estimated by RPS to the analytical values for the SS L=8 Ising Model, normalized by the value of the analytical result at each point. The states in extremes of the energy are unlikely to be obtained and as such have their DoS underestimated and may not even be visited giving a deviation of 1. While it is also possible to overestimate the DoS, obtaining the negative values of deviation seen near $E=-25$ in the inset of right graph of Fig.5.2. This is also exemplified in Fig.5.3, where the deviation is larger in the extremes of the energies. Furthermore, it shows that lower magnetizations converge slower, as $M=0$ has more of a deviation than that of $M=0.5$, this due to the larger number of possible states.

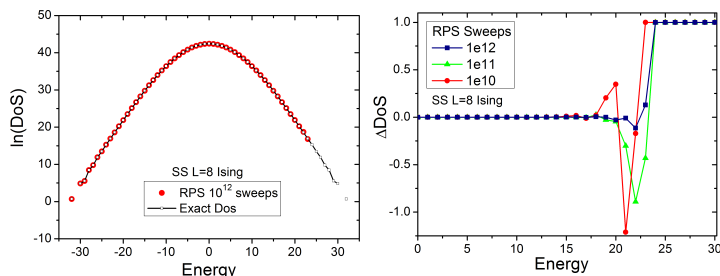


Figure 5.4: Plot of the normalized deviation of the RPS estimated DoS from the analytical solution [37] for the Simple Square Ising L=8.

One of the main properties of interest is the magnetization that minimizes the free energy as function of temperature M_{mF} . Insufficient sampling in RPS has a variety of effects in $F(M, T)$, namely the overall shape changes significantly and noise is present, this will change the apparent minima and modifies the shape of the $M_{mF}(T)$. Fig.5.5 shows the $F(M)$ curves for various temperatures at two different degrees of convergence and with the minima marked by open symbols. The corresponding $M_{mF}(T)$ curves are shown on the left of Fig.5.6, the difference in the curves is due to the noise in Fig.5.5, that results in false minima. Convergence of the magnetization curves is achieved at 10^9 repetitions, contrasting with the $2^N = 1.8 \times 10^{19}$ possible states for the system.

The general evolution of $F(M, T)$ is to converge from the extremes of M towards $M=0$ and at higher temperatures first, as can be seen in Fig.5.6. It should be noted that perfect

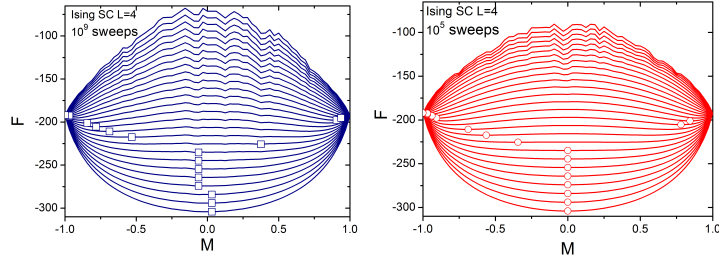


Figure 5.5: Shows the $F(M, T)$ isothermal curves for different degrees of convergence of the SC L=4 lattice, with the minima in respect to M denoted by a symbol. On the left 10^5 sweeps and on the right 10^9 .

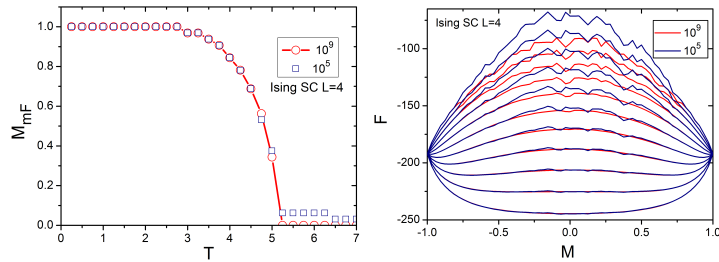


Figure 5.6: On the left is $M_{mF}(T)$ curves corresponding to the converged 10^9 curve in red circles and as blue squares the 10^5 sweeps that is not converged. The right plot contrasts the 10^9 and 10^5 $F(M, T)$ to show the evolution of convergence.

convergence of the whole of $F(M, T)$ is not a requirement, but rather that the minima must be well represented so that the $M(T)$ curve itself converges. In fact, while low T curves are impractical to converge fully near $M=0$, they correspond to a mostly aligned ferromagnetic state and thus have their $M \approx \pm 1$ minima well represented without full convergence.

The partition function also allows to determine the thermal mean magnetization $\langle |M| \rangle$ by using

$$\langle |M| \rangle = \sum_k \sum_i |M_k| \frac{g_i(E, M) e^{(E_i - HM_k)/\beta}}{Z}. \quad (5.1)$$

As mentioned before, $\langle |M| \rangle$ has a broader transition than M_{mF} and hence less of interest for the size of systems currently applicable to the method. Convergence of $\langle |M| \rangle$ however, is not dependent on the noise in the free energy and converges up to an order of magnitude faster. The left-most plot in Fig.5.7 presents the normalized deviation from the largest sampling (10^{13}) for a series of smaller runs. The middle and right side are the $M_{mF}(T)$ and $\langle |M| \rangle(T)$ plots comparing the 10^{12} and 10^{13} , $\langle |M| \rangle$ is already converged contrasting with the $M_{mF}(T)$ curve.

As RPS is based on generation of random configurations it is expected that away from convergence low probability states can be given a larger statistical weight. Filtering these low probability states was found to lower the noise. Fig.5.8 on the left shows the reduction of noise for a not yet converged $F(M, T)$ curve near T_c , with the minimum shown as a symbol. The curve by removing states with a sampling of 1 in 10^6 sweeps, has a minima closer to that of the converged 10^9 , than the original 10^6 curve. However, care needs to be taken as

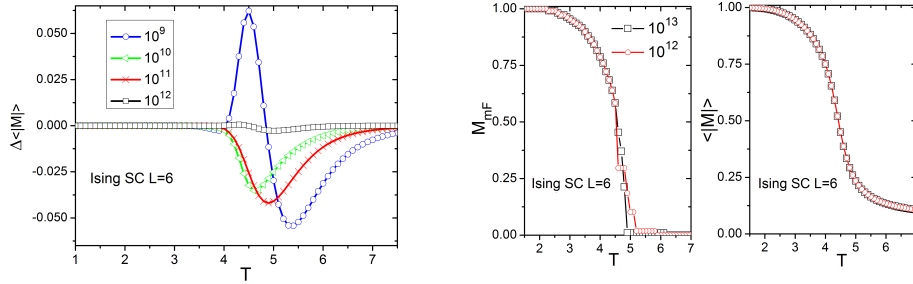


Figure 5.7: The left-most plot shows the convergence of $\langle |M| \rangle(T)$ as a function of lattice sweeps. The centre is the $M_{mF}(T)$ curve at 10^{12} and 10^{13} sweeps, the corresponding plot for $\langle |M| \rangle$ is shown on the right side graph.

excessive filtering changes the overall shape of the curve even if the smoothness of M_{mF} is improved, as shown for the filter 20 out of 10^6 . In the right plot are the $M_{mF}(T)$ curves that correspond to the runs shown on the left.

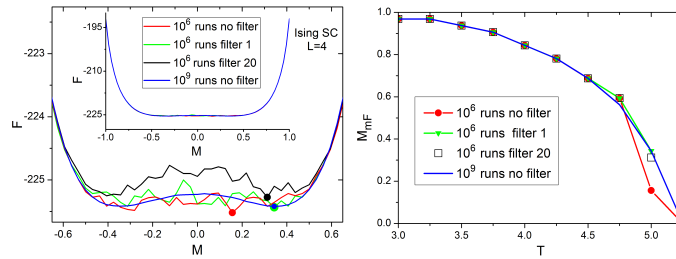


Figure 5.8: Left shows $F(M, T)$ curve at $T=5$ for different filter values for 10^6 and with a converged 10^9 run, with the minima in respect to M denoted by a symbol, the inset is the curve at the whole magnetization range. Right plot shows the corresponding $M_{mF}(T)$ curves.

Since we are sampling the possible configurations its natural for convergence to depend on the number of spins, however it will also depend on the number of nearest-neighbours for the system. Fig.5.9 compares the Body Centered Cubic (BCC) and Hexagonal Closed Packed (HCP) lattices with the same number of spins, but where as BCC has 8 nearest neighbours HCP has 12. The larger number of neighbours increases the quantity of possible energy states, requiring a larger sampling to describe the JDoS.

5.3 Fitting Free Energy

Given that the noise in the $F(M, T)$ curves is the primary deterrent in convergence of the $M_{mF}(T)$ curve, the possibility of fitting is of natural interest. The fitting chosen is based on the Landau expansion of free energy, motivated by the greater physical significance than an arbitrary, purely mathematical, fit.

In Landau theory the free energy is expressed as an expansion in a power series of an order parameter around the critical point. The free energy is assumed to be an analytical function in respect to the order parameter at the critical point. For a ferromagnetic system

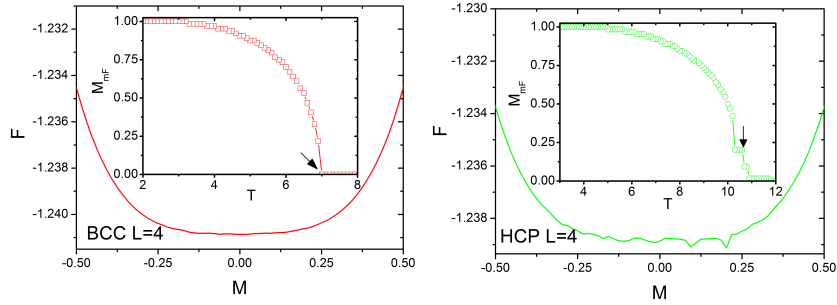


Figure 5.9: $F(M)$ plots at the respective T_c , showing the noise of the curve, the inset shows the $M(T)$ curve with an arrow pointing to the T_c . On the right is the HCP lattice and the left is the BCC, both with 10^{11} repetitions and 128 spins.

the order parameter is the magnetization and the free energy has the general expression of

$$F = -HM + \frac{1}{2}A(T)M^2 + \frac{1}{4}B(T)M^4 + \dots \quad (5.2)$$

Fig.5.10 shows that the Landau fit describes the $F(M, T)$ accurately for both non-converged (left) and converged (right) plots. The $M_{mF}(T)$ curve from the minima of the fit has a marked improvement on the non-converged sampling as seen on the right of Fig.5.11. However, while the $M_{mF}(T)$ curve from the non-converged free energy is closer to the expected curve because of elimination of false minima from noise, the overall shape of $F(M, T)$ is still not converged and the real minima are not represented as can be seen of the left side of Fig.5.11 for $T=5$.

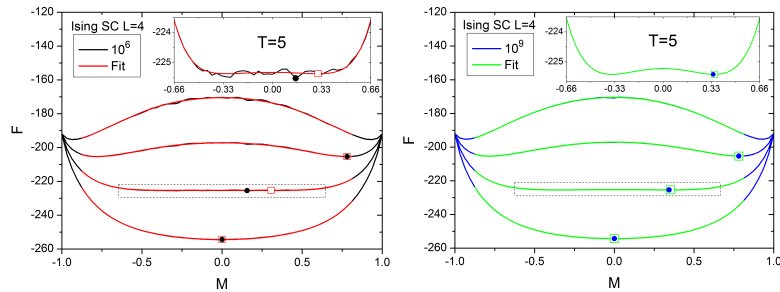


Figure 5.10: The $F(M, T)$ curves and their Landau fit for 10^6 (left) and 10^9 (right), the minima are shown by a square symbol for fit and circle for original curve. The insets are the zoomed in curve for $T=5$, that is denoted by the dashed box on the main graphs.

As Landau Theory consists of a power series in M higher magnetizations will require additional terms. Hence, a cut-off to M for the fit is needed and adding more terms will allow to fit to higher M values. However, the trade-off is that the resulting curve will be fitted to the noise, as more complex shapes of curves becomes possible with more terms. Another advantage is that the available magnetization values are continuous, while the M_{mF} is discrete since the number of magnetizations states of a finite lattice is itself finite.

The coefficients of the Landau expansion up to the 6th order for the SC $L=4$ lattice are shown in Fig.5.12, the grey dash line denotes the temperature at which the magnetization exceeded the cut-off of 0.75. At lower temperatures than the one denoted by grey line the fit

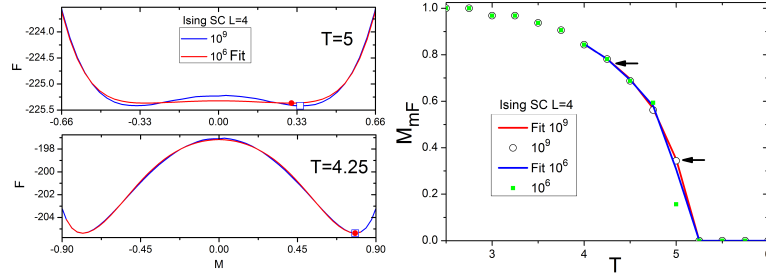


Figure 5.11: On the left the comparison of the fit at 10^6 runs and the corresponding $F(M, T)$ curve at 10^9 for $T=5$ (top) and $T=4.25$ (bottom). On the right, the respective magnetization curves.

no longer describes the system, and should not be trusted as representative of its behaviour. The change of signal of the A coefficient indicates the phase transition.

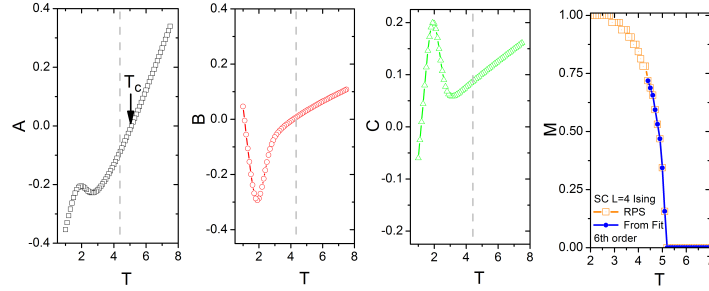


Figure 5.12: Landau coefficients as a function of temperature for the SC L=4 Ising System, with expansion up to the 6th order.

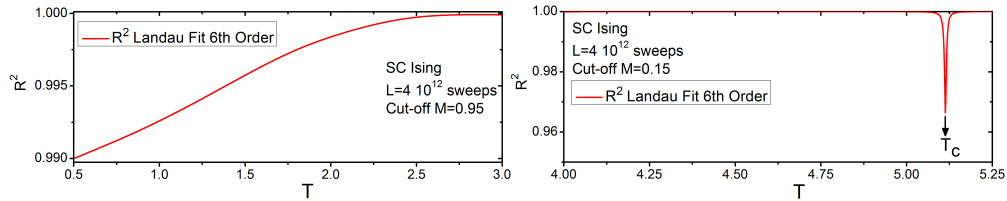


Figure 5.13: Quality fit factor R^2 as a function of temperature. The deviation at low temperatures due to saturation is on the left. On the right, the peak corresponding to T_c is shown.

Aside from the limitation of the expansion to reproduce the low temperature behaviour, the Landau fit will deviate from the free energy near T_c . This is a direct consequence of the critical behaviour of a Landau series being mean-field, that belongs to a different universality class than the Ising model. Since the deviation will only hold for the immediacy of T_c , the overall thermodynamic behaviour will not be affected and hence the system remains non-mean-field. The R^2 quality of fit for the Ising L=4 SC model with 10^{12} sweeps can be seen in Fig.5.13. The right plot corresponds to temperatures near T_c . In its turn, the deviation at low temperature as the system saturates is shown on the left graph.

Chapter 6

Application

Building on the established methodology and results from previous chapters, the Magnetocaloric Effect is explored, in addition to the compressible Ising model and the dependence of coercivity on temperature for the Ising model with single-ion anisotropy.

6.1 Thermodynamics

The advantage of determining the JDoS is that the thermodynamics becomes fully available, with temperature and field effects easily described. This is imperative in calculations of the thermodynamic properties that require a rich variety of points from the (T,H) degrees of freedom. This is readily obtainable as can be seen in Fig.[6.1,6.2], that show typical curves of interest in magnetism for M_{mF} of the SC L=6.

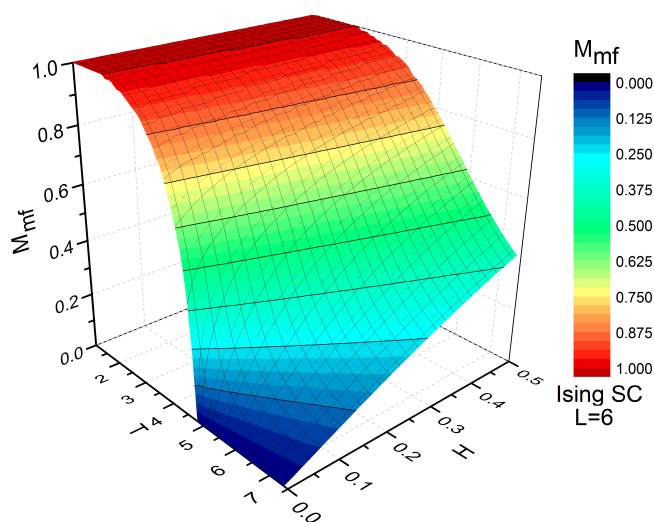


Figure 6.1: Plot of $M_{mF}(H,T)$ 3D curve of the L=6 Ising SC.

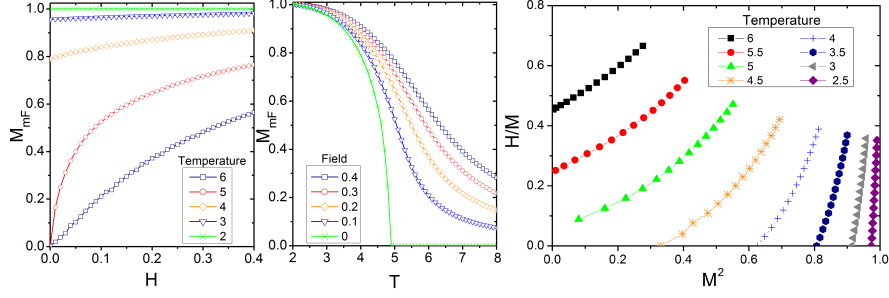


Figure 6.2: On the left, the $M(H)$ where the curves at the paramagnetic phase start at $M=0$, and ferromagnetic isotherms below $T_c=4.9$ have spontaneous magnetization. The centre plot are the isofield $M_{mF}(T)$ curves for SC $L=6$. The right plot is the respective Arrott plot showing H/M versus M^2 , the paramagnetic phase has curves that have $M^2=0$ when H/M is 0, implying that $M=0$ for $H=0$.

6.2 Magnetocaloric effect

In general, when a magnetic system is adiabatically ($\Delta S=0$) taken to a magnetized state by the application of a magnetic field the associated entropy S_M is lowered as the magnetic moments are aligned. Consequently, the temperature increases to the effect that the total entropy will be constant. If the field is then removed in an adiabatic fashion, the magnetic contribution to the entropy is lowered and the temperature has a corresponding decrease. This is called the Magnetocaloric effect (MCE) [41]. The quantities of interest in such processes are the isothermal variation of magnetic entropy ΔS_{MT} and the adiabatic temperature variation ΔT_{ad} .

The Maxwell relation gives that

$$\left(\frac{\partial S_M}{\partial H}\right)_{T,P} = \left(\frac{\partial M}{\partial T}\right)_{H,P}, \quad (6.1)$$

and thus the ΔS_{MT} can be obtained by

$$\Delta S_{MT}(H,T) = \int_{H_f}^{H_i} \left(\frac{\partial M}{\partial T}\right)_{H,P} dH, \quad (6.2)$$

however the latter equation can only be evaluated numerically in simulations such that

$$\Delta S_{MT}(H,T) = \sum_i \frac{M_{i+1}(T_{i+1}, H) - M_i(T_i, H)}{T_{i+1} - T_i} \Delta H, \quad (6.3)$$

the accuracy of the above result will depend on the points available for the calculation, that can be arbitrarily large in RPS. By it is part ΔT_{ad} can be obtained from the magnetic contribution to the heat capacity at constant pressure and field $C'_{P,H}$

$$C'_{P,H} = T \left(\frac{\partial S_M}{\partial T}\right)_{P,H}, \quad (6.4)$$

that can be rewritten along with the Maxwell relation to give

$$dS_M(H, T) = \frac{C'_H(T, M)}{T} dT + \left(\frac{\partial S_M}{\partial H} \right)_T dH, \quad (6.5)$$

and finally noting that $\Delta S = 0$ in an adiabatic process,

$$\Delta T_{ad} = - \int_{H_i}^{H_f} \frac{T}{C_P(T, H)} \left(\frac{\partial M}{\partial T} \right)_H dH. \quad (6.6)$$

Fig.6.3 contrasts the ΔS_M from the average magnetization $\langle M \rangle$, which does not vanish for $H < 0$, and M_{mF} for the L=6 SC lattice in RPS. The mismatch comes from the differences in both temperature and field behaviour between the two quantities. However, both have a peak at T_c , where the derivative of magnetization is larger and thus by Eq.(6.2) the ΔS_M is greater. It is expected that the peak of ΔS_M from M_{mF} is not as large as the infinite lattice, as the transition in the $M(T)$ is not as sharp. Nonetheless, the general features of a transition are well described using M_{mF} , within the available system sizes and will be the quantity of interest for MCE in this work. The heat capacity C_p from averaged quantities is shown on the left of Fig.(6.4), along with the T_{ad} from $\langle M \rangle$.

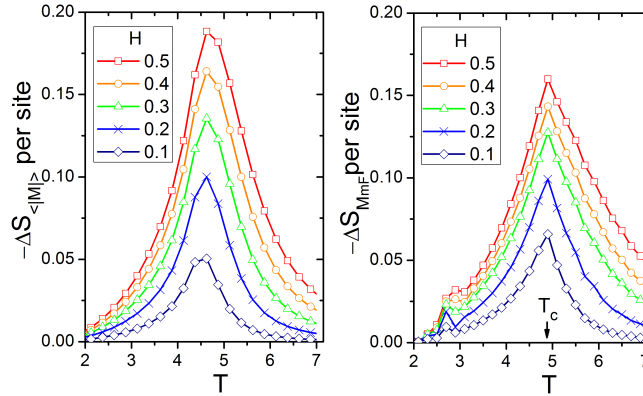


Figure 6.3: The two plots contrast the ΔS_M from $\langle M \rangle$ (left) and M_{mF} (right), using Eq.6.3

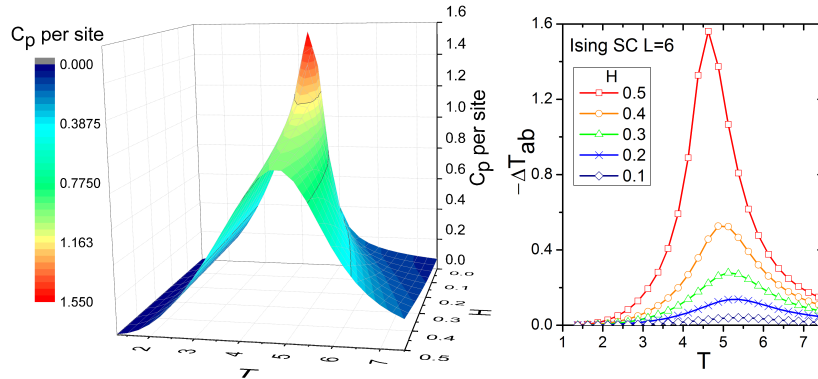


Figure 6.4: On the left, the surface plot of the heat capacity per site with dependence on field and temperature. On the right, the corresponding ΔT_{ad} from $\langle M \rangle$ (right).

6.3 Compressible Ising Model

The volume/pressure dependent behaviour of the exchange interaction and hence the Curie temperature is complex. When the ratio of the interatomic distance and the diameter of the unfilled inner shell d (or $4f$ shell) is large the exchange interaction is typically ferromagnetic. The exchange has a maximum value at a certain ratio and above it the J value drops off until it vanishes, while below it the trend is toward antiferromagnetic behaviour [42]. As such the dependence of J (and T_c) with compression/pressure depends if the system is below or above the maximum value. For instance metallic Cobalt increases in T_c with pressure, while the opposite is true for Gadolinium.

C. Domb [43] showed that in a compressible Ising model where the exchange depends on volume the transition can be of the 1st order. Bean and Rodbell [44] studied the thermodynamics of molecular-field magnetic systems with volume (v) magneto-volume coupling. Namely, by allowing T_c to vary with volume, such that $T_c = T_0[1 + \beta(v - v_0)/v_0]$ where T_0 is the critical temperature at the starting volume v_0 . It was shown that above a critical value of $\eta = 1$, where η is dependent on pressure, compressibility and β , the transition is of the 1st order.

This work adopts a Hamiltonian that depends of volume change (Δv) to describe a compressible Ising model, in the form of

$$\mathcal{H} = -J(\Delta v) \sum_{\langle ij \rangle} S_i \cdot S_j + K\Delta v^2, \quad (6.7)$$

where K is the elastic constant and $J(\Delta v)$ is linear. The $K\Delta v^2$ term represents the energy cost of compressing the lattice of a real world material, that for sufficiently small distortions obeys a second degree polynomial.

The behaviour of the system will then depend on the K constant and the dependence of J with Δv , that is assumed to be linear. If the $K\Delta v^2$ is dominant and the system will act like a rigid lattice, however as K is reduced the $M(T)$ curve changes shape. Eventually, the T_c value itself changes and the transition shows 1st order behaviour. This mirrors the results of Bean and Rodbell and can be understood noting that the Currie temperature is closely related to the exchange constant. Furthermore, the role of pressure and compressibility is analogous to the elastic energy term, it is then natural that interaction of K and J slope parallels the behaviour of the Bean-Rodbell model, in respect to the T_c slope and pressure/compressibility respectively. Fig.6.5 on the left shows how the $M(T)$ curve of the compressible Ising SC L=6 lattice changes with K at the same dJ/dv . The Bean-Rodbell model is shown on the right, for several η values.

The evolution of the nature of the transition can be elucidated by looking at the B coefficient in the Landau fit. When B is negative at T_c and C is positive the system has a metastable minima, leading to a discontinuous jump in magnetization once $M=0$ is no longer the minima. In Fig.6.6 the B coefficients are plotted in respect to temperature, for several of the curves in Fig.6.5. The high K values have positive B coefficients at T_c , as seen on both plots on the right. The right top plot has the intermediate case, where T_c changes but the transition is still close to 2nd order, with B having nearly vanished. The left top plot is the fully 1st order case.

A comparison of the $M(T)$ and $M(H)$ plots for the 1st order elastic and rigid SC L=6 lattices is shown in Fig.6.7. The discontinuous jump in magnetization at the zero field $M(T)$

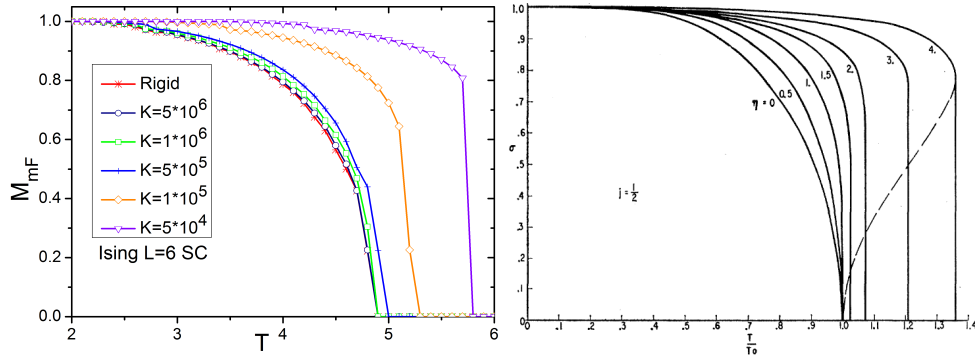


Figure 6.5: At the left, $M_{mF}(T)$ curves of the Ising SC L=6 for several elastic coefficients K for the same $J(\Delta v)$. On the right, the Bean-Rodbell model with $M(T)$ at different parameters η that depends on pressure, compressibility and T_c slope [44]. Above $\eta = 1$ the system has a 1st order transition.

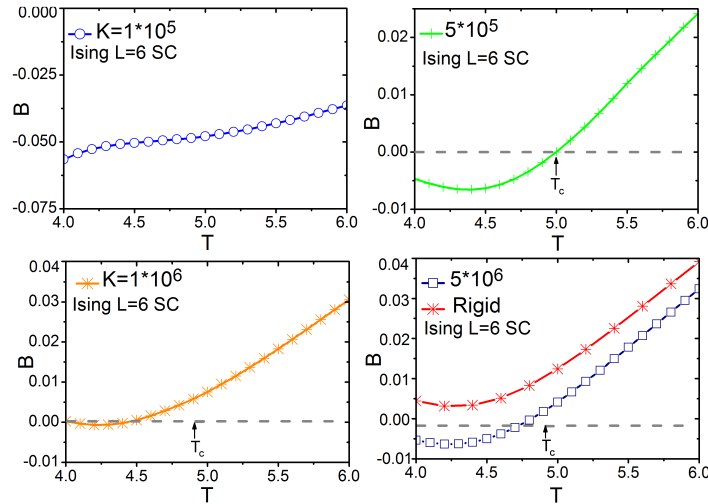


Figure 6.6: The B coefficients of the Landau Expansion as function of temperature for various curves in Fig.6.5 for the Ising SC L=6.

(right side) curve for the elastic lattice evidences a 1st order transition. Likewise, the inflection at the $M(H, T=6)$ curve (left side) is a sign of the 1st order nature of the system. The 1st order transition in the magnetization has its origin in a discontinuous change of the volume and hence J values. The system will change in volume continuously until T_c , at which point the lowest free energy corresponds to a significantly smaller volume, this is exemplified in Fig.6.8. The preference for a lower J value and hence volume, arises from the zero magnetization above T_c . As the orientation of the spins is no longer ordered, the value of $\sum_{\langle ij \rangle} S_i \cdot S_j$ is lowered and the magnetic energy from a high J cannot compensate for the energy cost of the larger volume distortion. Consequently, the smaller volume becomes preferable despite the lower J value. In the same line of thought, the J dependency with field and temperature mirrors the behaviour of the magnetization. As an increase of magnetization makes it energetically favourable to further enhance J , as seen on the $v(T)$ and $v(H)$ curves in Fig.6.9. The volume transition itself progressively takes more of a 1st order character, with the discontinuity in

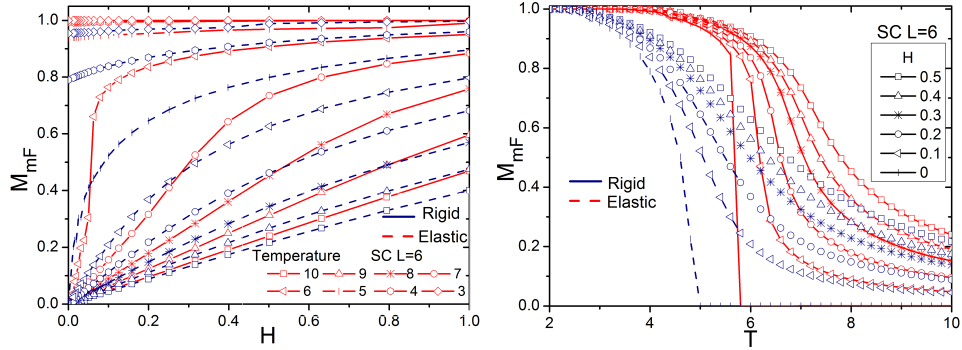


Figure 6.7: Left graph shows the $M_{mF}(H)$ isothermal curves for Ising SC $L=6$, the red lines are the elastic system and the dashed blue lines are for the rigid system. The right side are the corresponding $M_{mF}(T)$ isofield lines.

volume becoming more pronounced. This is replicated in Fig.6.8 on the right, for different K values.

While the discussion has focused on changing values of K at the same J slope, the same results are returned when fixing K and having the J slope as a variable. An increase in $\Delta J/\Delta v$ is analogous to a decrease in K . Seeing as the negative term for the magnetic energy is enhanced it can compete with the cost associated with a larger volume. While an exact condition for a 1st order transition is not discussed here, it would be possible to make a $(K, \Delta J/\Delta v)$ phase diagram, with some limitations due to finite magnetization steps and noise in the $F(M, T)$ curve.

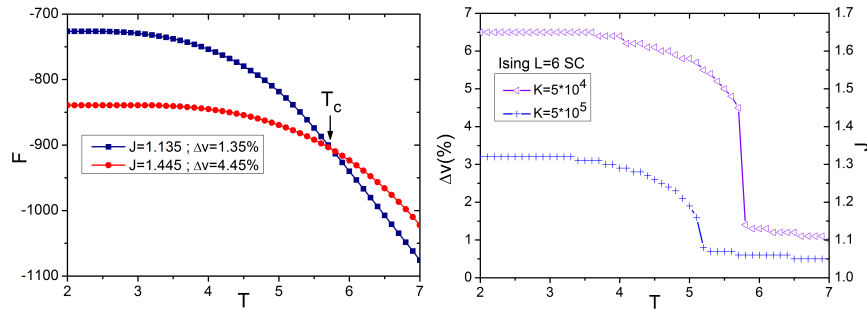


Figure 6.8: The left plot shows the free energy as function of temperature, for the volumes before and after T_c of Fig.6.7. The right plot shows the volume transition for various K values, in Fig.6.5.

Magneto-volume coupling can play a critical role in real world materials for MCE applications that have a 1st order volume transition. Using the above methodology these transitions can be studied. The discontinuity in magnetization for 1st order transitions can enhance the MCE. Recalling Eq.(6.2), ΔS depends on the derivative of the magnetization in respect to temperature, thus it can be enhanced for 1st order transitions. This can be seen geometrically, as the numerical evaluation of Eq.(6.2) is related to the area between isothermal curves in the $M(H)$, that is increased near T_c , as seen in the elastic system of Fig.6.7 on the $M(H)$ plot. The corresponding ΔS is seen in Fig.6.10 for both the elastic and rigid lattices, the

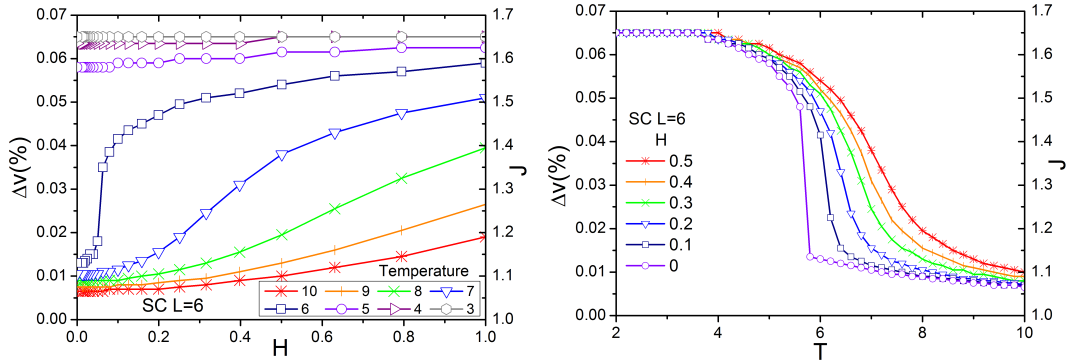


Figure 6.9: The volume and J behaviour in isothermal (left) and isofield (right) curves.

maximum value of ΔS is increased by 40%.

In an analogous fashion, structural transitions could be approached by comparing the energies of two lattices and finding the one with the lowest energy structure for a given set of (T, H) values, allowing potentially to find the critical fields and temperatures for the transition. The application of similar Hamiltonian as above, will be seen later on for a discrete Heisenberg-like model for Gadolinium, emphasising the generality of studying systems using the JDoS.

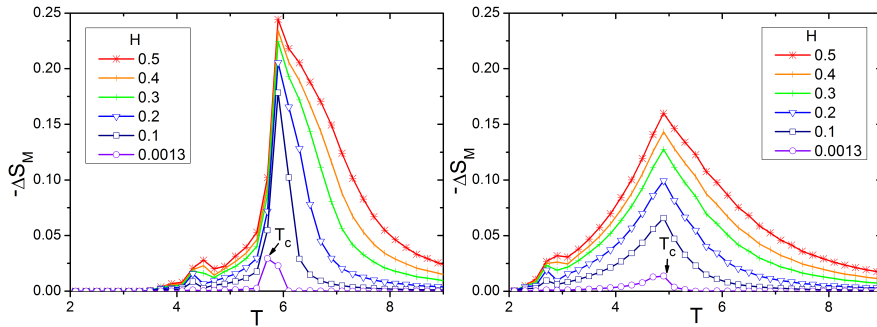


Figure 6.10: On the left, the $\Delta S_M(T)$ plot for the MCE effect from M_{mF} on the elastic SC $L=6$ lattice. On the right side the same for the rigid system.

6.4 Magnetic Anisotropy Energy

In the majority of magnetic materials a significant contribution to the anisotropy comes from the competing effects of electrostatic crystal-field interaction and relativistic spin-orbit coupling. The crystal-field leads to a quenching of orbital moment, due to the energy level splitting. However, spin-orbit coupling is favoured by a larger orbital moment. When an axial crystal field is relatively weak compared with the spin-orbit coupling, but such that the separation between the low-lying split energy levels is higher than $k_B T$, the orientation of the moments is restricted to the z axis [45]. The effective behaviour is of a Heisenberg model

with a anisotropy term

$$\mathcal{H} = -J \sum_{\langle ij \rangle} \hat{S}_i \cdot \hat{S}_j - D \sum_i S_i^2, \quad (6.8)$$

which is the case for Dy^{3+} . Further, if the D term is sufficiently high an Ising Model behaviour is expected.

Since $-D \sum_i S_i^2$ term is homogeneous it can freely be added to the partition function if written using JDoS. A hysteresis loop plots the magnetization values as a function of magnetic field from negative to positive values. For a sufficiently large field value the magnetization saturates aligned with the field. At the coercive field value the magnetization vanishes even in the ferromagnetic phase. Fig.6.11 shows the evolution of the hysteresis loop with temperature, for the Ising SC $L=6$ with $D=0.1$ on the left-most plot. At low temperatures the system saturates at lower fields and has a broader loop corresponding to large coercive fields. When the temperatures are higher larger fields are needed for saturation and the coercivity is lowered with loop the becoming narrower.

In the paramagnetic phase without MAE ($D = 0$) there is no coercivity or spontaneous magnetization, as can be seen on the middle plot of Fig.6.11. Upon introduction of anisotropy the loop broadens and coercivity is present ($D = 0.5$). In contrast, below T_c the system is ferromagnetic and coercivity does not vanish for $D=0$ (on the far right).

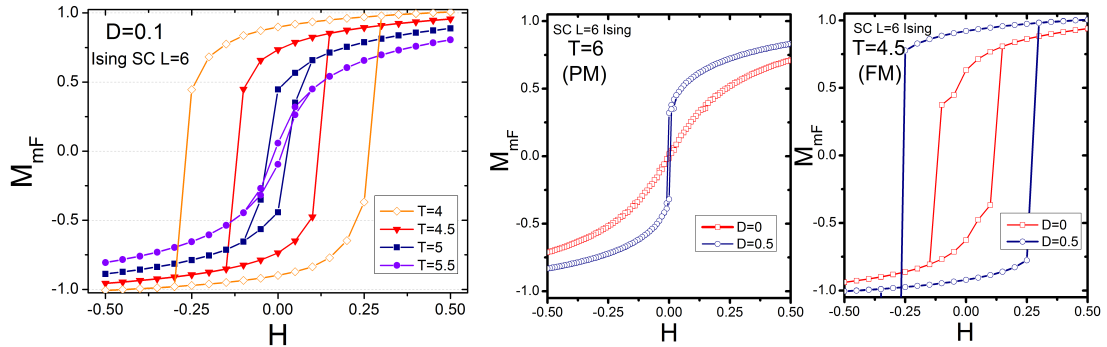


Figure 6.11: On the far left, hysteresis loops for the SC Ising $L=6$ lattice for various temperatures. The other hysteresis loops show varying D values. On the middle is the system above T_c on the paramagnetic phase. The right plot corresponds to the ferromagnetic phase.

Chapter 7

Generalization of RPS to the Heisenberg Model

7.1 Introduction

As RPS samples states to form a histogram and normalizes entries based on possible configurations at a given magnetization, these states must be discrete. Discretization of the Heisenberg model is not widely discussed in literature [10]. An immediate difference is that excitations no longer an infinitesimal energy cost. Rapaport reported that a Metropolis simulation of a 30 direction Heisenberg-like model was consistent with the T_c and magnetization critical behaviour of the Heisenberg model proper [46]. A later paper by Margaritis et al. [47] took a theoretical point of view by using renormalization group theory. Namely they showed that the 12 (icosahedral), 20 (dodecahedral) and 30 (same as Rapaport) models belong to the same universality family. Arguing that this would indicate that the anisotropy operators that reduce the rotation symmetry of the Heisenberg model due to discretization would be irrelevant in 3D. This being indicative of all models belonging to the Heisenberg universality class. Fisch used a discretization in the study of cubic anisotropy in the Heisenberg model. Specifically, with 6 directions [48] and latter 12 orientations pointing to the middle of the edges of a cube, adding cubic anisotropy [49].

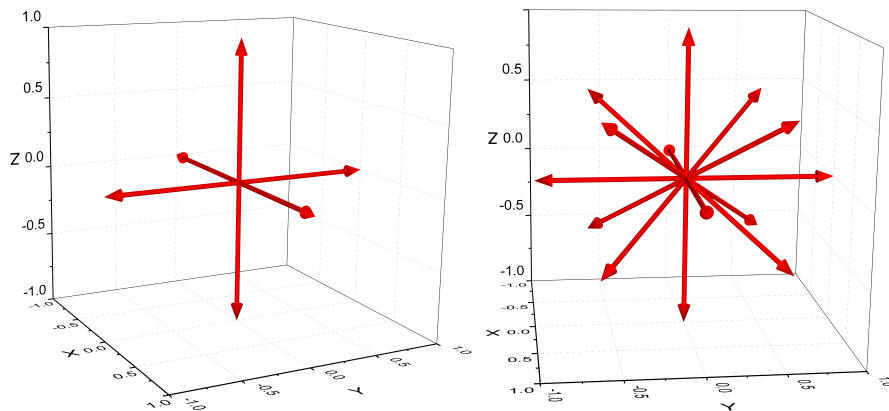


Figure 7.1: On the left the 6 direction discretization. On the right the 14 vector Heisenberg-like model.

In this work, the first discretization chosen was the 6 directions corresponding to the both orientations in the x,y or z axis as shown in Fig.7.1. However, it was found to be inept as the transition for the SC was of the 1st order, a result that which was later found to have been shown by Fisch [48]. The 1st order transition can be verified in the $F(M, T)$ curves, where a metastable minima exists in the paramagnetic phase which becomes the global minimum at T_c , meaning that the magnetization varies discontinuously at T_c . This behaviour is shown in Fig.7.2, on the left is the plot of $F(M, T)$ with squares denoting the minima for temperatures near the transition. The minimum goes from $M \approx 0$ to $M \approx 0.75$, that results in the jump in the $M_{mF}(T)$ plot on the right. The T_c of 1.7-1.8 agrees well with the reported value of 1.62 [48].

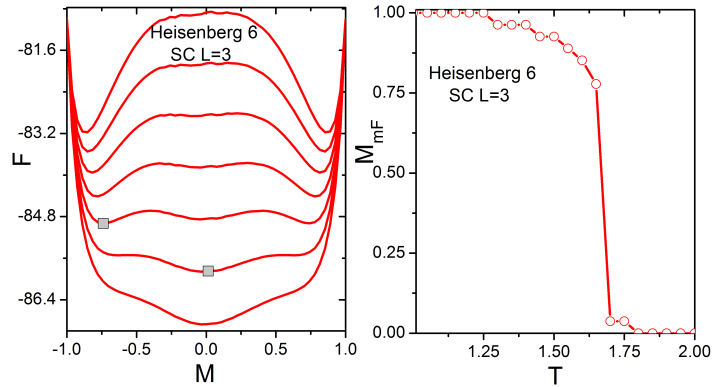


Figure 7.2: On the left $F(M, T)$ curves for the SC L=3 Heisenberg Model, the squares mark the minima immediately before and after T_c , showing the discontinuous jump in magnetization. On the right is the corresponding $M_{mF}(T)$ curve.

Table 7.1: Orientations for the Heisenberg 14 model, the plane denotes the directions with equal M_z .

x	y	z	Plane
0	0	1	0
$\sqrt{6}/4$	$\sqrt{6}/4$	0.5	1
$\sqrt{6}/4$	$-\sqrt{6}/4$	0.5	1
$-\sqrt{6}/4$	$-\sqrt{6}/4$	0.5	1
$-\sqrt{6}/4$	$\sqrt{6}/4$	0.5	1
1	0	0	2
0	1	0	2
-1	0	0	2
0	-1	0	2
$\sqrt{6}/4$	$\sqrt{6}/4$	-0.5	3
$\sqrt{6}/4$	$-\sqrt{6}/4$	-0.5	3
$-\sqrt{6}/4$	$-\sqrt{6}/4$	-0.5	3
$-\sqrt{6}/4$	$\sqrt{6}/4$	-0.5	3
0	0	-1	4

Following the 6-direction discretization, a 14 vector discretization was chosen as shown in

table 7.1 and Fig.7.1 on the right, for convenience it will be referred to as Heis-14. The criteria was to have a regular magnetization step in the z-axis and similar solid angles. However, the chosen directions imply a reduced rotational symmetry, as taking the system such that the z-axis takes the place of the x or y axis is not an invariant operation, as would be the case of the isotropic Heisenberg model.

7.2 Algorithm

To accommodate the larger number of possible directions the algorithm must be modified. To store the direction at a given site the vectors to table 7.1 are numbered. The energy calculation is made by using a look-up table of the dot product of the possible interactions, using the directions of the neighbour site and the direction at the chosen site as indexes. The new algorithm is shown below.

```

for  $k$  < number of runs do
  set lattice array  $s$  to all up;
  create a random permutation of an array with the lattice sites repeated four times
  each;
  for  $i$  < size lattice*4 do
    let  $r$  be the  $i$ -th spin in the permutation;
    generate a random number from 0 to 3 and store to  $rng$ .
    use look-up table to determine the flip using the  $rng$  and  $s[r]$  as indexes;
    calculate  $E$  from flip;
     $h(M,E) \leftarrow h(M,E) + 0.5$ ;
  end for
end for
Return histogram;

```

An alternative C++ code was also developed, that relies on the sorting of an array of energy values. The interest arises from the possibility of added complexity to the Hamiltonian in the future. Specifically, accounting for different in-plane and out-of-plane exchange values in the HCP lattice, that is the case for Gd [50]. For this case the histogram of possible energies greatly increases in size surpassing by far current RAM sizes.

The workflow for this code differs in that it will only generate as many runs as it is possible to fit in memory and then output a histogram. Several histograms then have to be combined.

```

for  $k$  < runs do
  initialize lattice value;
  call the Fisher-Yates function;
  for  $i$  < size lattice*4 do
    get the  $i$ -th spin in the permutation and flip;
    calculate  $E$  from flip;
    array( $i$ )  $\leftarrow E$ ;
     $i \leftarrow i + 1$ ;
  end for

```

```

end for
call unique function and print h(E,M).

```

The unique function simply sorts the energies using the `std::sort` function from the C++ standard library and iterates over the result counting the frequency.

```

for  $M < \text{size lattice} * 4$  do
  sort[M*runs,(M+1)*runs[
  for  $k < \text{runs}-1$  do
    if  $E(k) == E(k+1)$  then
      count ← count + 1;
    else
      print E(k) and count;
      count ← 0;
    end if
  end for
  print E(k) and count;
  count ← 0;
end for

```

The resulting histograms are from a much smaller number of sweeps typically 10^6 or less compared to the 10^9 using the histogram in memory method. Thus the execution is typically done by a Bash script. The script calls the C++ executable a number of times (typically 100 times) and follows it up with a compacting C code. The C code reads the various histograms to memory, one magnetization value at a time and runs the unique function. The compaction step can be repeated for an increasing number of sweeps as desired, until it becomes computationally inexpensive to call a Matlab scrip that outputs the final result.

In the case of in-plane and out-of-plane anisotropic exchange, the array of energies becomes an array of structures, wherein a variable for in-plane (E_{ip}) and out-of-plane (E_{oop}) energies are defined. The sorting function must also accommodate this change, as such a user defined comparison function is passed to `std::sort`, such that the final array is sort both in respect to E_{ip} and E_{oop} . The resulting intermediate histogram file sizes increase substantially and great care must be given towards optimizing the input for the compilation executables, as to minimize the computational time. This is currently a work in progress.

Contrasting with the Ising model, the energy values will no longer be integers and the histogram quickly becomes larger than memory. One possibility is to use energy binning by limiting the decimal precision of the dot product.

7.3 Results

The behaviour of the 14 discretization Heisenberg model for the SC lattice is not unambiguous. At 10^{12} sweeps of the $L=4$ lattice a steep transition appears near $T=0.9$, although the $F(M, T)$ is still noisy and far away from convergence. Indeed even a small filtering will change the behaviour dramatically, with the transition becoming continuous and the $T_C \approx 1.3$ being close to the continuous model value of [51]. Caution with filtering is important however, as it will not be clear whether the low probability states are overestimated or are required to describe the system. It is possible that both transitions are in fact present, as Fisch [48]

did find that a discontinuous transition was present near $T=1.15$ by means of simulations, in addition to the typical Heisenberg transition. While the 12 direction model used by Fisch incorporated cubic anisotropy due to the discretization not present here, the paper did put forward a justification to the effect based on mean-field theory and suggested that this would hold true even for the 30 direction model at temperatures that were not simulated by Rapaport. The $\langle|M|\rangle$ and M_{mF} plots with and without filtering are contrasted in Fig.7.3. The figures with the expected transition are on the right and where made filtering the states with ≤ 5 sampling in 10^{12} , however even 1 in 10^{12} would suffice.

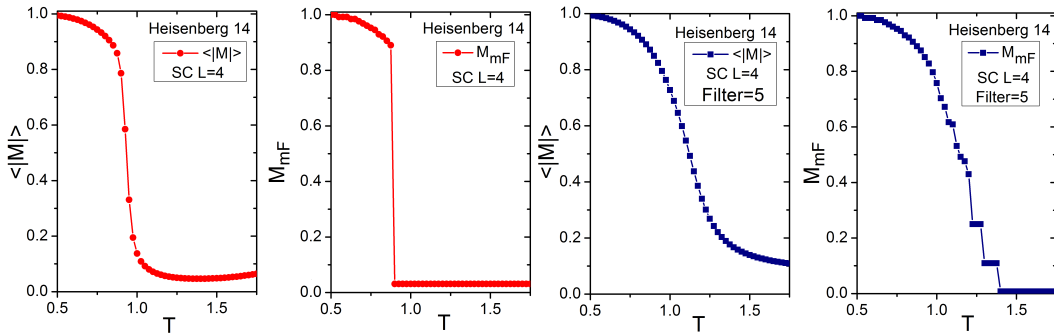


Figure 7.3: On left most plot is the $\langle|M|\rangle(T)$ that shows the steep transition and the its respective $M_{mF}(T)$ plot on the centre left. The $\langle|M|\rangle(T)$ and $M_{mF}(T)$ plots on the centre right and far-right are for the filtered calculation.

The logarithm of the JDoS for the SC lattice in the Heisenberg 14 discretization is shown in Fig.7.4 of the left, with the corresponding contour plot on the right.

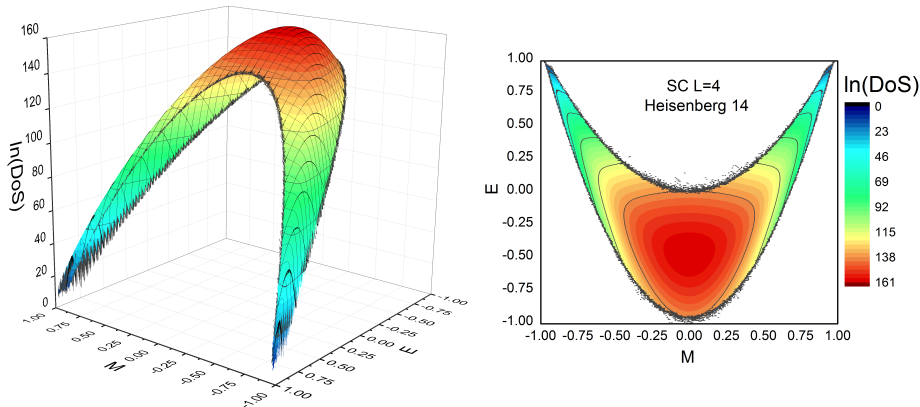


Figure 7.4: Logarithm of the JDoS for the SC Heisenberg 14 model. The left side is the 3D plot and its corresponding contour is on the right.

The $M_{mF}(T)$ curves for the HCP and SC lattices are plotted in Fig.7.5, using filtering and fitting. The theoretical T_c 's for the infinite lattices from high-temperature expansion are indicated by an arrow. The discrete model values have transitions at temperatures that are lower than the continuous model proper. This is unusual as one would expect that finite size effects would result in a higher T_c . However since the Rapaport and the 12-direction Fisch model had transitions near the theoretical value, it is unlikely that a larger lattice would not trend to the theoretical value.

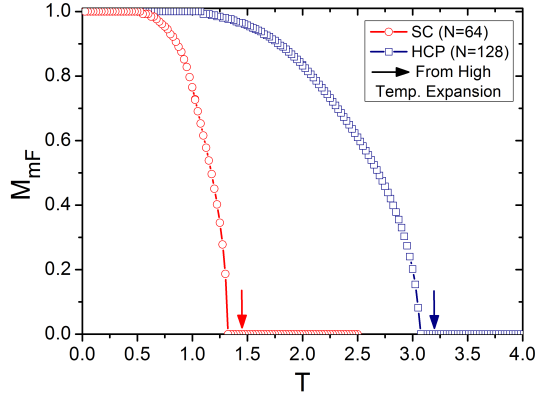


Figure 7.5: $M_{mF}(T)$ plots for the HCP and SC Heisenberg 14-discretization, with filtering and Landau Fitting. The arrows indicate the theoretical T_c [51].

7.4 Comparison

To better understand the Heisenberg-like model described above, a variety of Metropolis simulations were performed. Of principle interest are the effects of the discretization, the nature of the transition for the SC lattice and the differences between M_z and $\langle M \rangle = \sqrt{S_x^2 + S_y^2 + S_z^2}$. The simulations were carried out for the Heisenberg 14 with the previously indicated directions, as well as a more isotropic choice of vectors and the Rapaport model, using Metropolis single update code by the author. The modified Heis-14 has the z component of the diagonal directions changed so that it makes a 45° angle at the z axis.

As a starting point, the continuous Heisenberg model will be compared with Heis14. As previously mentioned the continuous Heisenberg model has infinitesimal excitations, in other words for any non vanishing temperature value it is possible for the system to have spins that are not fully aligned. This is in contrast with the Ising model where the system is saturated well above $T=0$, as the energy cost of change in direction is discrete. It is then immediate that the Heis14 cannot have the same low-temperature behaviour as the continuous system, as it is discrete. The behaviour above T_c can still be comparable at high-temperatures. Fig.7.6 on the left shows simulations for the continuous Heisenberg model and the Heis14 for both RPS and Metropolis simulation with the modified vectors. The difference between both SC $L=50$ lattices becomes noticeable above $M=0.5$, the continuous model is slower to saturate due to the possible infinitesimal change in spin orientation. Additional simulations in the Rapaport model (not pictured) confirm that the saturation behaviour would not replicate the continuous system even at 30 possible directions.

The RPS calculation is harder to compare due to the different T_c , for clarity the right side shows the same plot but with the scale adjusted to $T_c - T$, based on the T_c for each $M(T)$ curve. This graph also shows that M_z from the free energy minima has a similar behaviour to the conventional $\langle M \rangle$ quantity. It should also be noted that this is not solely a limitation of RPS as Zhou et al. [29] also used M_z as the magnetization parameter in the Wang-Landau Heisenberg simulation for SC $L=10$.

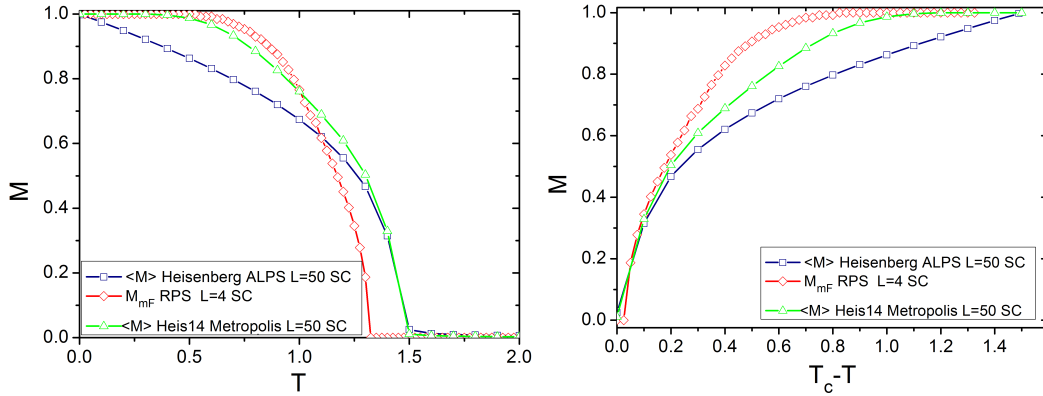


Figure 7.6: Both plots show the continuous Heisenberg model made in ALPS [21] and the Heis14 model with M_z in RPS (from M_{mF}) and $\langle M \rangle$ for Metropolis simulation. The right plot has the scale adjusted to better compare the curves.

As for the nature of the transition in discrete Heis14 model, it was not possible to verify it completely. The Metropolis simulations of the original Heis14 model used for RPS showed the steep transition, however when the modified directions were used the expected behaviour is observed. Both results are shown in Fig.7.7. It is possible that the original Heis14 has a more complex energy landscape than the more isotropic orientations and that the transition near $T=0.5$ is merely metastable. Moreover, all these discrete models proved difficult to simulate and depended heavily on the lattice initialization. When a single direction was chosen the curves were well behaved, however if the orientation of each spin was random the behaviour of the $M(T)$ curve was irregular.

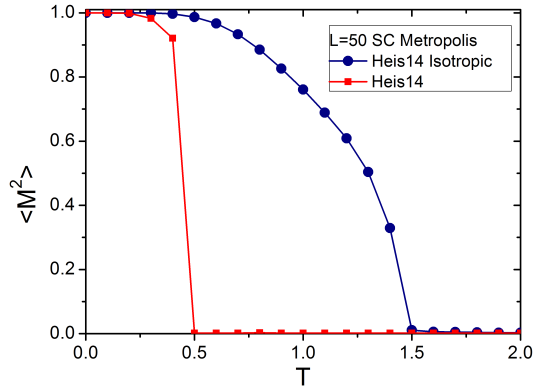


Figure 7.7: $\langle M \rangle(T)$ plots for SC L=50 Heis14 with original and modified directions, from Metropolis simulations.

Chapter 8

Application of the Heisenberg model

8.1 Simulation of Gd

Simulation of entropy change and magnetostriction of Gadolinium (Gd) was performed using the HCP Heisenberg 14 model. Gd was chosen a test system as a quality sample was available and the its structure (HCP) is rather simple. To determine the needed parameters of exchange constant and energy as a function of distortion, Density Functional Theory simulations were performed by Dr. João Gonçalves, using the Vienna Ab initio simulation package [52]-[55]. The exchange-correlation functionals used was the Perdew-Burke-Ernzerhof (PBE) [56] in the form of Generalized Gradient Approximation (GGA), with on-site Coulomb repulsion (+U) which is needed to accurately describe the exchange interactions [50].

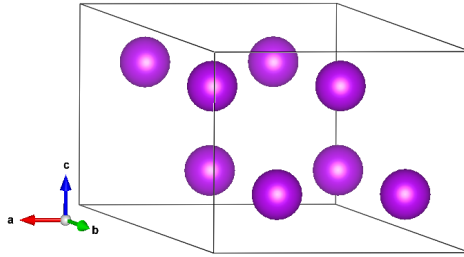


Figure 8.1: 2x2x1 Gd supercell used for calculations. Made using VESTA [57].

The exchange values were calculated by the energy differences from ferromagnetic (FM) and anti-ferromagnetic (AF) arrangements, that were parametrized to a Heisenberg model Hamiltonian, by fitting the energies as a function of the $\sum_{\langle ij \rangle} \hat{S}_i \cdot \hat{S}_j$, the slope then being J . The simulations were carried out in the spin-polarized mode on a 2x2x1 supercell with 8 atoms (Fig.8.1) with a 9x9x9 k-mesh. This was repeated for a variety of lattice distortions to determine the J value dependence with the lattice constants. Several AF and FM configurations were studied, up to 14 to test convergence. Additionally, total energy values for the unit cell were fitted to a second degree polynomial as function of lattice distortion (Fig.8.2). The k parameter for a distortion of the c axis was 2/3 of the value for the a axis, this motivated the RPS calculations be run at a fixed a axis.

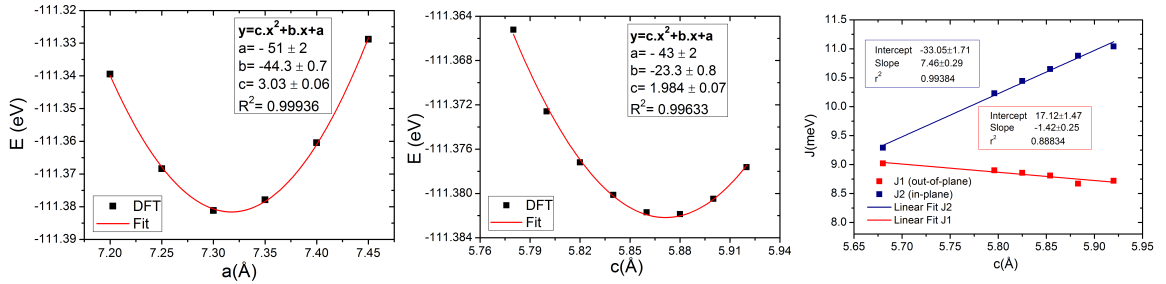


Figure 8.2: On the left, the total energy dependency on volume for Gd. Right side are the J values for the in-plane and out-of-plane interactions as a function of c -axis variation.

The experimental measurements were performed in Imperial College London in collaboration with Dr. Zsolt Gercsi, Dr. Karl Sandeman and Prof. Lesley Cohen. The magnetization measurements were performed on a Quantum Design Physical Properties measurement system (PPMS) and the measurement of volume change as function of temperature was carried out using a custom high sensitivity capacitance bridge system installed in the PPMS. The sample was a ultra-pure single Gd crystal made at Ames laboratory (Iowa State University) by Prof. Karl Gschneidner Jr. e Prof. Vitalij Pecharsky.

For the simulation the Hamiltonian was modified to introduce a coupling between J and lattice volume distortion, along with a spring constant term to account for the energy cost of lattice deformation, such that the Hamiltonian becomes

$$\mathcal{H} = -J(x) \sum_{\langle ij \rangle} \hat{S}_i \cdot \hat{S}_j + \frac{1}{2}k.x^2 - MH, \quad (8.1)$$

the k constant was obtained from the second degree polynomial fit of Fig.8.2 and x is the distortion along the c axis.

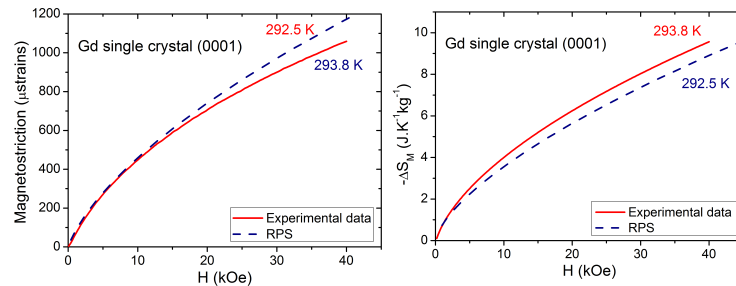


Figure 8.3: The left graph is the field dependent behaviour of magnetostriction both from experimental measurements and simulation for Gd, at $T \approx 293$. On the right, the magnetic entropy variation as a function of field for the same temperatures.

While the DFT calculations pointed to a J value of 9.69 meV and a dJ/dx of $18\text{meV}/dx$, this resulted in a T_c that is overestimated by 50 K, 16% of the experimental value of 290 K. To determine if the model was sufficient to describe the system values were chosen to best agree with the experimental T_c , giving $J=8.3$ and a dJ/dx of $24\text{meV}/dx$. Given that the exchange parameters are dependent of the $+U$ parameter that is not known experimentally and that the J value being used is equal for in-plane and out-of-plane nearest neighbour interactions,

these make for reasonable values. The simulation was performed in under 1 hour on a single desktop CPU, using HCP $N=128$ with 10^{11} sweeps. The resulting $M(T)$ and $M(H)$ plots are shown in Fig.8.4, along with the experimental data. The agreement is quite reasonable until higher magnetizations of around 100 emu/gram. This echoes the differences seen for the SC simulations between the continuous and discretized models in the previous chapter, where at low temperatures the two models differ.

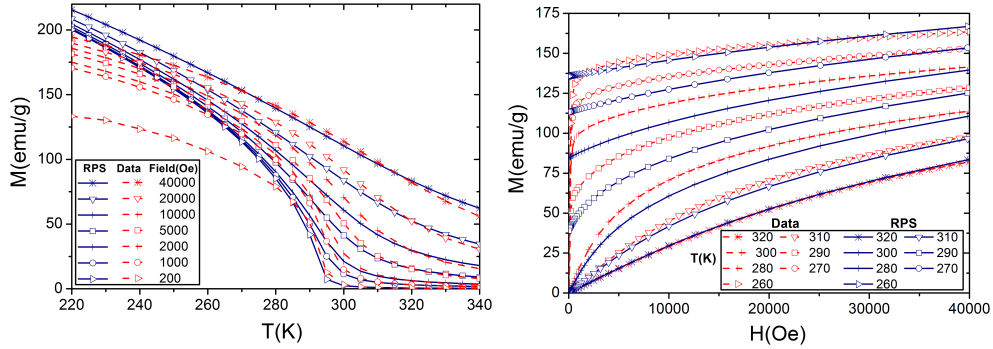


Figure 8.4: The graphs show the experimental and simulated magnetization at different field-temperature values. On the left is the $M(T)$ plot and on right is the $M(H)$ plot.

The simulated strain induced as function of field (magnetostriction) and the experimental values (measured along the c axis) are shown on the left side of Fig.8.3, the corresponding ΔS_M dependency on field is shown on the right.

Fig.8.5 plots the isofield magnetostriction (on the left) and ΔS_M (right side) as functions of temperature.

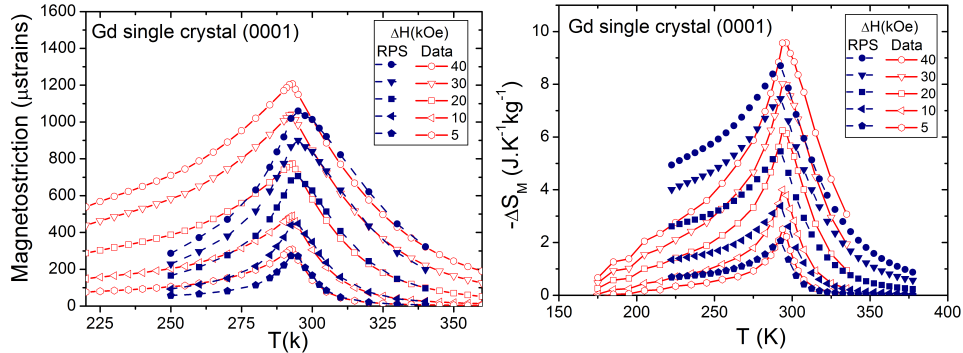


Figure 8.5: On the left, the isofield curves of the magnetostriction as function of temperature for experimental and simulated data. The right plot is the same for the variation in magnetic entropy.

The plots agree quite well despite the various approximations and somewhat small size of the lattice. The peaks of both ΔS_M and the magnetostriction isofields are underestimated by $\approx 10\%$ and the difference becomes larger at lower temperatures. If the effects of the discretization are taken into account it is clear that the Hamiltonian describes the system well. Despite the differences, the MCE is well represented, and this methodology may prove useful for fast estimation of even rather complex thermodynamic behaviours at a minimal computational cost.

Chapter 9

Conclusions

The particulars of the recently proposed Random Path Sampling method were explored. The convergence of averaged properties, along with the novel quantity of magnetization from the free energy minimum M_{mF} was studied. Additionally, enhancements to the method such as Landau Fitting and filtering were demonstrated and shown to reduce the number of sweeps needed to converge M_{mF} by up to 3 orders of magnitude.

CPU and GPU codes were developed with significant performance gains, aiming towards a greater performance that utilizes the embarrassingly parallel nature of the method.

Exploiting the capabilities of RPS the thermodynamic behaviour of the Ising model was discussed, with focus on the Magnetocaloric Effect. A compressible Ising model along the lines of what was proposed by Domb was approached and shown to follow the general nature of the Bean-Rodbell molecular-field model. Further, the temperature dependence of the coercivity for the Ising model with single-ion anisotropy was exemplified.

A generalization of RPS was made by applying it to a discretized Heisenberg-like model with 14 directions. Using the fast estimation capabilities of RPS, the magnetostriction and Magnetocaloric Effect in Gadolinium were simulated, with a wall time of approximately an hour on a desktop computer. The results were in reasonable agreement with the experimental data, within the limitations of the model used. The general methodology used here may open up the possibility of fast computational simulations of the thermodynamics of magnetic materials.

A treatment of other vector models, namely the Potts model would be possible in the framework of RPS and may be pursued in the future.

A possible avenue of interest would be different starting states for the sampling, to improve the sampling of low and high energy states. An additional path for improvement might be the binning of energies for systems where the histogram is too large for memory. However, this requires a systematic study of the effects of the size of the bins.

Bibliography

- [1] Pappon P., Leblond J., Meijer P.H.E. and Schnur S.L., *The Physics of Phase Transitions Concepts and Applications*, Springer, 2nd Edition 2010;
- [2] Ising, E., *Beitrag zur Theorie des Ferromagnetismus*, Zeitschrift für Physik 31 (1925);
- [3] Niss M., *History of the Lenz-Ising Model 1920-1950: From Ferromagnetic to Cooperative Phenomena*, Archive for History of Exact Sciences 59-3 pp.267-318 (2004);
- [4] Peierls R. E., *On Isings Model of Ferromagnetism*, Proceedings of the Cambridge Philosophical Society 32, pp.477-481 (1936b);
- [5] Bragg W. L. and Williams E. J., *The Effect of Thermal Agitation on Atomic Arrangement in Alloys*, Proceedings of the Royal Society A 145, pp.699-730 (1934);
- [6] Bethe, H. A. *Statistical Theory of Superlattices*, Proceedings of the Royal Society [A] 150, pp.552-575 (1935);
- [7] Fowler R. H., *Adsorption Isotherms. Critical Conditions*, Proceedings of the Cambridge Philosophical Society 32, 1441-151 (1936);
- [8] Onsager L., *Crystal Statistics. I. A Two-Dimensional Model with an Order-Disorder Transition*, Physical Review 65-3& 4 pp.117-149 (1944);
- [9] Onsager L. , *Autobiographical Commentary of Lars Onsager*, in Mills, Ascher and Jaffee (1971), pp. xix-xxiv (1947);
- [10] Landau D. P. and Binder K., *A Guide to Monte Carlo Simulations in Statistical Physics*, Cambridge University Press, 2nd Edition 2005;
- [11] Pelissetto A. and Vicari E. *Critical phenomena and renormalization-group theory*, Physics Reports 368 pp.549-727 (2002);
- [12] Weiss P., *"L'hypothèse du champ moléculaire et la propriété ferromagnétique"*, Journal de Physique Théorique et Appliquée 6 pp.661-690 (1907);
- [13] Suwa Y., Okamoto M. and Hamada T., *First-principles Materials-simulation Technology*, Hitachi Review 63-9 (2014);
- [14] Liechtenstein A.I., Katsnelson M.I., Antropov V.P. and Gubanov V.A. *Local spin density functional approach to the theory of exchange interactions in ferromagnetic metals and alloys*, Journal of Magnetism and Magnetic Materials 67-1 pp.65-74 (1987);

- [15] Curtarolo S., Hart G.L.W, Nardelli M. B., Mingo N., Sanvito S. and Levy O., *The high-throughput highway to computational materials design*, Nature Materials 12 pp191-201 (2013);
- [16] Sokolovskiy, V., Buchelnikov, V., Skokov, K., Gutfleisch, O., Karpenkov, D., Koshkid'ko, Yu, Miki, H., Dubenko, I., Ali, Naushad, Stadler, S. and Khovaylo, V. , *Magnetocaloric and Magnetic Properties of Ni₂Mn_{1-x}Cu_xGa Heusler Alloys: an Insight from the Direct Measurements and ab initio and Monte Carlo Calculations*, Journal of Applied Physics 114 (2013);
- [17] Oitmaa J., Hamer C. and Zheng W., *Series Expansion Methods For Strongly Interacting Lattice Models*, Cambridge University Press, 1st Edition 2006;
- [18] Ritchie D. S. and Fisher M. E., *Theory of Critical-Point Scattering and Correlations. II. Heisenberg Models*, Physical Review B 5-7 (1972);
- [19] Beale P. D., *Exact Distribution of Energies in the Two-Dimensional Ising Model*, Physical Review Letters 76-1 (1972);
- [20] Zhuravlev K. K. , *Molecular-field theory method for evaluating critical points of the Ising model*, Physical Review E 72 (2005);
- [21] B. Bauer et al. (ALPS collaboration), *The ALPS project release 2.0: open source software for strongly correlated systems*, Journal Statistical Mechanics P05001 (2011);
- [22] Metropolis N., Rosenbluth A.W., Rosenbluth M.N., Teller A.H. and Teller E, *Equations of State Calculations by Fast Computing Machines*, Journal of Chemical Physics 21-6 pp.10871092 (1953);
- [23] Swendsen R.H., Wang J. S. and Ferrenberg A. M. *New Monte Carlo Methods for Improved Efficiency of Computer Simulations in Statistical Mechanics* in *The Monte Carlo Method in Condensed Matter Physics* ed: Binder K., Springer 2nd Edition 1995;
- [24] Swendsen R. H. and Wang J.-S. , *Nonuniversal critical dynamics in Monte Carlo simulations*, Physical Review Letters, 58-2 pp.8688 (1987);
- [25] Wolff U. , *Collective Monte Carlo Updating for Spin Systems*, Physical Review Letters 62-4 (1989);
- [26] Ferrenberg A. M. and Landau D. P., *Critical behaviour of the three-dimensional Ising model: A high-resolution Monte Carlo study*, Physical Review B 44, 5081 (1991);
- [27] Wang F. and Landau D. P., *Efficient, Multiple-Range Random Walk Algorithm to Calculate the Density of States*, Physical Review Letters 86 pp.2050-2053 (2001);
- [28] Tsai S-H, Wang F. and Landau D. P., *Critical endpoint behavior in an asymmetric Ising model: Application of Wang-Landau sampling to calculate the density of states*, Physical Review E 75 pp.61108-61117 (2007);
- [29] Zhou C., Schulthess T.C., Torbrügge S. and Landau D. P., *Wang-Landau Algorithm for Continuous Models and Joint Density of States*, Physical Review Letters 96 pp.120201-120205 (2006);

- [30] Eisenbach M., Nicholson D.M., Rusanu A. and Brown G., *First principles calculation of finite temperature magnetism in Fe and Fe₃C*, Journal of Applied Physics 109 pp.07E138 (2011);
- [31] Amaral J.S., Goncalves J.N. and Amaral V.S. *Thermodynamics of the 2-D Ising Model From a Random Path Sampling Method*, IEEE Transactions on Magnetics 50-11 (2014);
- [32] Saito M. and Matsumoto M., *SIMD-Oriented Fast Mersenne Twister: a 128-bit Pseudorandom Number Generator in Monte Carlo and Quasi-Monte Carlo Methods (2006)*;
- [33] Preis T., Virnau P., Paul W. and Schneider J. J., *GPU accelerated Monte Carlo simulation of the 2D and 3D Ising model*, Journal of Computational Physics (2009);
- [34] Weigeland M. and Yavorskii T., *GPU accelerated Monte Carlo simulations of lattice spin models*, Physics Procedia 15 (2011);
- [35] Cook S., *CUDA Programming A Developer's Guide To Parallel Computing with GPUs*, ed: Binder K., Elsevier (2013);
- [36] <http://docs.nvidia.com/cuda/curand/>. Last accessed 3/9/2015;
- [37] Beale P. D. .Retrieved from: <http://spot.colorado.edu/~beale/index1.html>;
- [38] Ferreira A.L.C and Toral R., *Projected single-spin-flip dynamics in the Ising model*, Physical Review E 76 (2007);
- [39] Wang J.-S., Tay T. K . and Swendsen R. H., *Transition Matrix Monte Carlo Reweighting and Dynamics*, Physical Review Letters 82-3 (1999);
- [40] Wang J.-S. and Swendsen R. H., *Transition Matrix Monte Carlo Method*, Journal of Statistical Physics 106 (2002);
- [41] Gschneidner K. A. Jr., Pecharsky V. K. and Tsokol A. O., *Recent developments in magnetocaloric materials*, Reports on Progress in Physics 68 pp.1479-1539 (2005);
- [42] Patrick L., *"The Change of Ferromagnetic Curie Points with Hydrostatic Pressure"*, Physical Review 93-3 pp.384-492 (1953);
- [43] Domb C., *"Specific Heats of Compressible Lattices and the Theory of Melting"*, The Journal of Chemical Physics 25 (1956);
- [44] Bean C. P. and Rodbell D. S., *"Magnetic Disorder as a First-Order Phase Transformation"*, Physical Review 126-1 (1961)
- [45] De Jongh L. J. and Miedema A. R. ,*Experiments on simple magnetic model systems*, Advances in Physics 50-8 (2001);
- [46] Rapaport D. C., *A discrete vector spin model*, Journal of Physics A: Mathematical and General 18 (1985);
- [47] Margaritis A., Odor G. and Patkós, *Sequence of discrete spin models approximating the classical Heisenberg ferromagnet* , Journal of Physics A: Mathematical and General 20 (1987);

- [48] Fisch R., *Cubic models with random anisotropy*, Physical Review B 48-21 (1993);
- [49] Fisch R., *Power-law correlations and orientational glass in random-field Heisenberg models*, Physical Review B 57-1 (1998);
- [50] Turek I., Kudrnovsky J., Bihlmayer G. and Blugel S., *Ab initio theory of exchange interactions and Curie temperature of bulk Gd*, Journal of Physics: Condensed Matter 15 pp.2771-2782 (2003);
- [51] Ritchie D. S. and Fisher M. E. , *Theory of Critical-Point Scattering and Correlations. II. Heisenberg Models*, Journal (1972);
- [52] Kresse G. and Hafner J. , *Ab initio molecular dynamics for liquid metals*, Physical Review B 47:558 (1993);
- [53] Kresse G. and Hafner J., *Ab initio molecular-dynamics simulation of the liquid-metal-amorphous-semiconductor transition in germanium*, Physical Review B 49:14251 (1994);
- [54] Kresse G. and Furthmüller J. , *Efficiency of ab-initio total energy calculations for metals and semiconductors using a plane-wave basis set*, Computational Material Science 6:15 (1996);
- [55] G. Kresse and J. Furthmüller. *Efficient iterative schemes for ab initio total-energy calculations using a plane-wave basis set. Physical Review B*, 54:11169 (1996);
- [56] Perdew J. P., Burke K., and Ernzerhof M., *Generalized Gradient Approximation Made Simple*, Physics Review Letters 77, 3865 (1997);
- [57] Momma K. and Izumi F., *"VESTA 3 for three-dimensional visualization of crystal, volumetric and morphology data"*, Journal of Applied Crystallography, 44 pp.1272-1276 (2011);